Clinical and experimental molecular and multimodality imaging studies in B cell malignant lymphomas

(Klinikai és kísérletes, molekuláris és multimodalitású képalkotó vizsgálatok B sejtes malignus lymphomában)

Doctoral (Ph.D.) – thesis

Dr. Zsombor Ritter

University of Pécs, Clinical Centre, Department of Medical Imaging

Head of Doctoral School of Health Sciences: Prof. Dr. József Bódis

Programme leader of Doctoral School of Health Sciences: Prof. Dr. István Kiss

Supervisor of Doctoral School of Health Sciences: Prof. Dr. Katalin Zámbó and Dr. Hussain Alizadeh

University of Pécs, Faculty of Health Sciences

Doctoral School of Health Sciences

Pécs, 2022

Contents

1 Abbrevations

PET/CT - Positron emission tomography/X-ray computed tomography

FDG - 2-deoxy-2-[^{18}F]fluoro-D-glucose

^{67}Ga-citrate - Gallium[^{67}Ga];2-hydroxypropane-1,2,3-tricarboxylate

NHL - Non-Hodgins's lymphoma

DLBCL - Diffuse large B-cell lymphoma

R-CHOP - Rituximab, Cyclophosphamide, doxorubicin hydrochloride (Hydroxydaunorubicin), vincristine sulfate (Oncovin), and Prednisone

LDH - Lactate dehydrogenase enzyme

B2M - Beta-2-microglobulin

EBV - Epstein-Barr Virus

GC - Germinal centre

ABC - Activated B-cell

GLUT1-7 - Glucose Transporter proteins

SPECT - Single photon emission computed tomography

IBSI - Imaging Biomarker Standardization Initiative

Bc.DLFL1 - the name of the lymphoma mouse model

CLI - Cerenkov luminescence imaging

MRI - Magnetic Resonance Imaging

ECOG - The Eastern Cooperative Oncology Group

R-IPI - Revised International Prognostic Index

EFS - Event-free survival

CR - Complete response

PR - Partial response

PD - Progression

SUV - Standardised uptake value

VOI - Volume of interest

TLG - Total Lesion Glycolysis

TMTV - Total Metabolic Tumor Volume

NGTDM - Neighborhood gray-tone difference matrix

GLCM - Gray-level co-occurrence matrix

GLRLM - Grey level run length matrix

GLSZM - Grey level size zone matrix

ML - machine learning

AUC - Area under the receiver operator characteristics curve

H&E - Haematoxylin-eosin

CFSE - 5-6-carboxyfluorescein succinimidyl ester

FITC – Flurescein-5-isothiocyanate

ARG - Autoradiography

ROC - Receiver Operator Characteristics Curve

mLNs - Mesenteric lymph nodes

COO - Cell of origin

WHO - World Health Organization

ALARA - As low as reasonably achievable

MDA - Minimal detectable activity

2 Foreword

Nuclear medicine methods allow non-invasive investigation of biological processes. Hungarian-born researcher György Hevesy laid the foundations of radiolabelling, for which he was awarded the Nobel Prize in 1943. In the last 20-30 years, a number of new radiopharmaceuticals have appeared and novel imaging methods have evolved.

The development of PET (positron emission tomography) diagnostics has made it possible to characterise many diseases more accurately. Nowadays, FDG-PET/CT scans are the mainstay of many tumour diseases, including lymphoma. Over the last two decades, FDG-PET/CT examinations has become routine in the investigation of staging and in the follow-up of therapy.

Based on the literature, we can now significantly influence therapy using nuclear medicine methods in many disease groups, therefore these methods can be the cornerstones for personalized medicine.

When a new method or therapeutic option is introduced, preclinical studies must be always carried out. We have been able to reproduce and develop precision nuclear medicine methods in rodent models for more than two decades. Thus, the ultimate beneficiary of preclinical studies is the patient.

The applied radiopharmaceuticals -FDG (2-deoxy-2-[^{18}F]fluoro-D-glucose) and ^{67}Ga-citrate (gallium[^{67}Ga];2-hydroxypropane-1,2,3-tricarboxylate)- in the present studies and their measurement methods and capabilities are identical in human and preclinical studies. Therefore, the preclinical experimental data obtained using these radiopharmaceuticals can be potentially useful in a clinical setting.

My work included clinical and preclinical studies, which are described in detail below.

3 Introduction - Focus on Lymphoma diagnostics

Haematological malignancies can occur at various life stages throughout age groups. Non-Hodgkins's lymphoma (NHL) is globally the most common hematological malignancy, accounting for nearly 3% of cancer diagnoses and deaths [1]. The non-Hodgkin lymphomas are a diverse group of malignancies about 80% of which are of B-cell origin in the Western hemisphere. The most common histologic subtype in adults worldwide is diffuse large B-cell lymphoma (DLBCL) composing about 30%-40% of NHLs diagnosed worldwide each year [2, 3]. Around half of the morbidities occur in the age group of patients older than 60 years [1-3].

Diffuse large B-cell lymphomas are a particularly heterogeneous group of lymphoproliferative neoplasms [2, 4] with different biology, clinical presentations, and response to treatment [4, 5]. For an effective therapeutic strategy, it is important to understand their heterogeneous phenotypes.

Although outcomes for patients with DLBCL improved significantly with the addition of Rituximab to the standard chemotherapy backbone over a decade ago, they have largely remained stable since that time. Approximately 40 % of DLBCL patients will develop relapsed or refractory disease [6, 7]. Most patients in this setting succumb to their disease despite salvage treatments, suggesting that the highest impact area for improvement is first-line therapy [8]. Summarizing DLBCL is potentially curable with standard treatment in approximately 60% of cases. Standard treatment includes Rituximab, cyclophosphamide, doxorubicin hydrochloride (hydroxydaunorubicin), vincristine sulfate (Oncovin), and prednisone (R-CHOP). About 25%-30% of patients are resistant to standard chemo-immunotherapy, therefore other therapeutic approach is utilized, namely 20% of patients are treated with salvage therapy including high dose therapy and autologous hematopoietic stem cell transplantation [4, 9, 10].

Recent advances in molecular characterization techniques have deepened the understanding of the biology of DLBCL and paved the way for personalized therapies aimed at improving outcomes in this disease. Advances on the understanding of the genetic landscape and molecular features of DLBCL have identified high-risk group with poor response to chemo-immunotherapy. There is an unmet clinical need to identify these high-risk patients as early as possible to apply targeted and more intensive therapy on individualized basis, as the majority of refractory or relapsed patients will eventually die from their disease.

3.1 Clinical management of DLBCL, pillars of diagnostics

The initial evaluation of DLBCL patients is aimed at determining the stage of the disease and assessing for end-organ damage either by the disease and/or by preexisting comorbid conditions. The workup in a patient with suspected lymphoma usually starts with comprehensive chemistry panel including complete blood counts with differentials, hemostasis parameters, renal function, hepatic function, lactate dehydrogenase enzyme (LDH), beta-2-microglobulin (B2M), hepatitis B, C, Epstein-Barr Virus (EBV) and human immunodeficiency viral serology. Lymph node biopsy is required to establish a definitive diagnosis of lymphoma; this should be an excisional biopsy rather than a needle biopsy, because nodal architecture is often difficult to assess when small amounts of tissue are used [11-13].

When only histopathological markers are used, germinal centre (GC) or non-GC phenotypes are distinguished. By genetic marker analysis of the cell of origin (COO), the other main DLBCL group besides GC is the activated B-cell (ABC) subtype. Patients within the ABC-COO group of DLBCL usually have lower clinical response rate and worse prognosis [3, 14, 15]. In recent years, new DLBCL subgroups have been created to provide more accurate classification and more accurate prognosis prediction with regards to response to therapy, based on special molecular genetic differences [3, 15] exploiting the possibility of detailed genomic characterization with next generation sequencing [5, 16].

After the histologic confirmation of DLBCL, imaging study is requested to assess the extent and stage of disease. The preferred imaging modality is functional imaging with FDG PET/CT.

FDG molecule is the most commonly used radiotracer in clinical nuclear medicine for diagnostic imaging being mostly transported to the cells via upregulated Glucose Transporter proteins (GLUT 1-7), (Figure 1.) [17, 18]. FDG- PET/CT in recent years has become the key component in diagnosing, including the staging of, patients with high-grade lymphoma, particularly diffuse large B-cell lymphoma and Hodgkin's lymphoma [19, 20]. This modality is the mostly used for monitoring the efficacy of therapy as well [19, 21, 22].

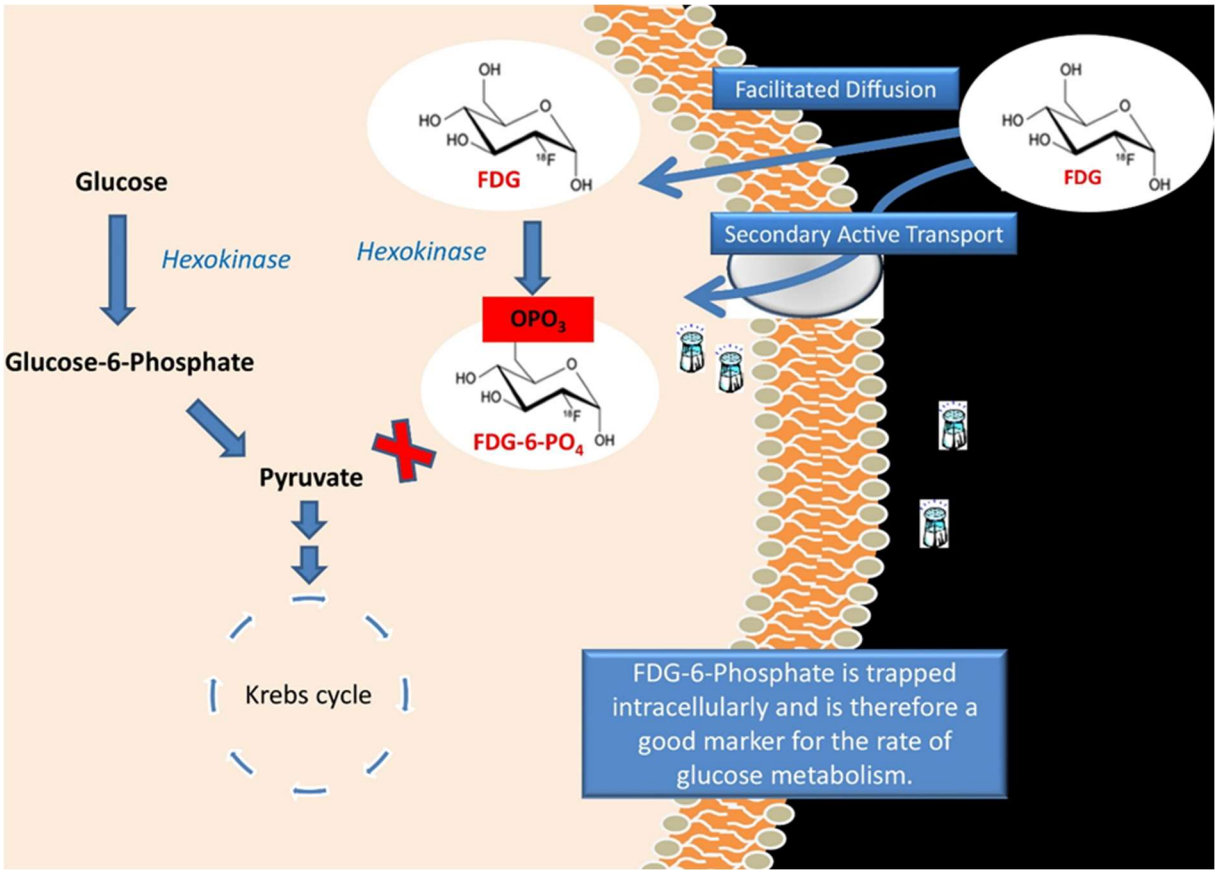

1. Figure 1: Uptake and metabolism of FDG in cells: after the radiotracer is entered into the cell, mainly through the GLUT transporters, hexokinase ad a phosphate group to FDG. Then the other enzymes of glycolysis no longer consider the phosphorylated FDG as a substrate, so it can not metabolised further. therefore it is trapped in the cell. *ref. http://doi.org/10.1148/rg.2018180072*

On the other hand - before the widespread availability of FDG - earlier clinical practice in diagnosis and therapeutic management of lymphomae extensively relied on ^{67}Ga-citrate single photon emission computed tomography (SPECT) and two-dimensional gamma scintigraphy with the same isotope. The diagnostic performance of FDG is superior to that of ^{67}Ga-citrate, however the relevance of ^{67}Ga imaging is somewhat still present in lymphoma (Figure 2). In addition to lymphoma diagnostics, ^{67}Ga is also increasingly viewed as a therapeutic isotope in oncology by virtue of its Auger-electron emission and specific lymphoma uptake.

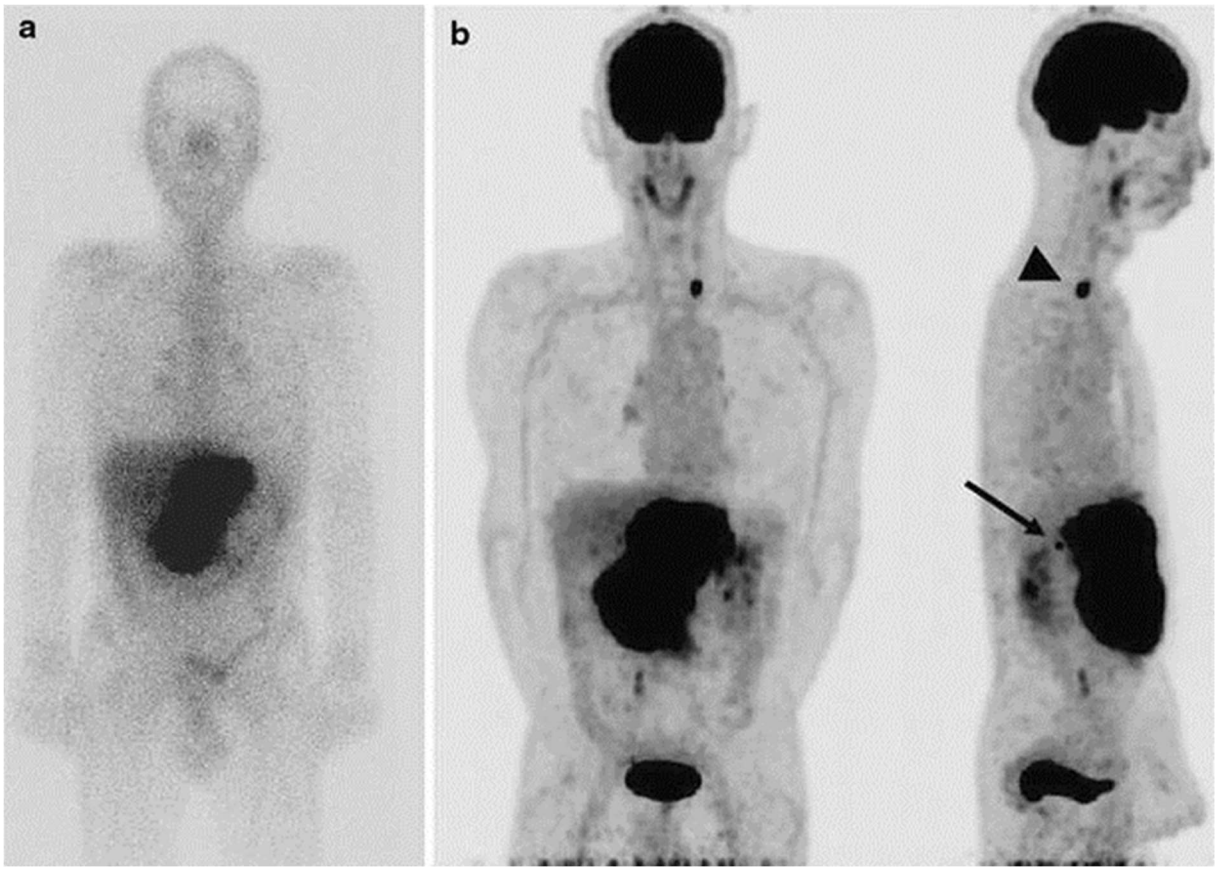

2. Figure 2: The sensitivity and specificity of FDG is much higher than ^{67}Ga-citrate scintigraphy. However, before the introduction of FDG, ^{67}Ga-citrate scintigraphy was the mostly applied radiotracer in the staging and follow up of lymphoma. The left supraclavicular lymph node could be detected well only on the FDG-PET/CT scans. a: ^{67}Ga scan, b: FDG scan. *ref: DOI 10.1007/s12149-011-0549-0*

3.2 The importance of radiomics derived from FDG-PET/CT in predicting the survival

Taking in consideration that about 25-30% of patients are primarily resistant to the current first-line treatment with rituximab based chemo-immunotherapy [23], identifying the high risk group which will do not respond, has very high priority.

In addition to histological approaches one of these modalities could be the use of conventional and textural parameters derived from the baseline FDG-PET/CT. Methods to individualize treatment choices are being increasingly employed in different clinical trials, yielding favourable correlations with improved response rates [5, 24]. Studies in the field of cancer imaging research have been actively engaged with radiomics in combination with machine learning [25].

Radiomics means the extraction of a large number of quantitative features from medical images using advanced mathematical analysis. With well determined image biomarkers, there is a possibility to characterize tumorous regions more deeply and get data which are invisible and unrecognizable for the human eye [26].

However, radiomics has been reported to be sensitive on various factors such as individual biology, acquisition protocols, choice of delineation, binning and resolution as well as calculation methods, which challenges prior studies to repeat [27]. Nevertheless, standardization proposals such as the Imaging Biomarker Standardization Initiative (IBSI) [28] support the endeavours to report findings in a repeatable way.

3.3 Preclinical studies 1: focus on Cerenkov Luminescence Imaging (CLI)

In connection with recent advances in lymphoma histology and in vivo imaging studies, in situ in vitro imaging imaging-based diagnostic tools have also evolved. The application of these emerging methods holds the promise of timely access to advanced differentiation of DLBCL patient clusters. The identified subgroups of patients would then benefit from quick and tailored immune- or intensive chemotherapy.

As earlier mentioned clinical management of the disease involves the evaluation of enlarged lymph nodes. Before starting definitive therapies, further excisional biopsy and detailed histological analysis of at least one accessible, tumorous part of a suspect lymph node is a mandatory step in the course of diagnostics [12, 13].

By localising involved lymph nodes, subsequent sampling could benefit from the use of the currently obligatory pre-therapy FDG-PET/CT or ^{67}Ga-citrate scan images to establish therapeutic directions. As an example, identifying, removing and analysing lymph nodes and inhomogeneous tumor masses using the available Cerenkov light emission of Fluorine-18 isotope after the PET/CT exam would lead to more precise molecular biology evaluation, hence leading to choosing a better therapeutic protocol.[20, 21, 29, 30].

In this direction, our group has previously described the Bc.DLFL1 tumor model as a spontaneous high-grade lymphoma isolated from BALB/c mice, which is reproducibly transplantable via intraperitoneal injection into syngeneic recipients. This model shows preferential tissue distribution to mesenteric lymph nodes and spleen during peritoneal spreading, and propagates via the lymphatic vessels [31]. This well-characterized lymphoma is a suitable model for preclinical investigations, including assessment of novel imaging

techniques [32]. The model invariably leads to death 21 days after the animals are inoculated, with 90% of animal deaths occurring between 11 and 14 days. Thus, animals are considered to be in early stage before 4 days of lymphoma administration, in advanced stage from day 7 and end-stage from day 11 post intraperitoneal inoculation.

The basic aim of this part of our work was to assess staging possibilities by imaging and monitoring dissemination of Bc.DLFL1 lymphoma in vivo with PET and SPECT and ex vivo with high resolution Cerenkov luminescence imaging (CLI).

CLI as an advanced imaging technique [33, 34] has a considerable potential for clinical translation. It is an optical imaging technique based on the emission of Cerenkov photons. The Cerenkov photons are emitted by charged particles such as electrons and positrons. It develops when the velocity of these particles is greater than the velocity of light in a medium (such as in water and tissues). Every new CLI application is of high medical interest, especially those using clinically authorised and marketed radiopharmaceuticals or isotopes. One such yet not reported isotope in practical CLI is ^{67}Ga. However, underreported, theoretical calculations show that the high-energy gamma photons emitted during the decay of this isotope could lead to secondary electrons resulting in Cerenkov luminescence in water or in water-containing tissues [17, 35].

3.4 Preclinical studies 2: the investigation of tumor spreading in early and advanced stage

After intraperitoneal inoculation of Bc.DLFL1, the lymphoma cells attach to lymphocyte-rich regions within the omentum and mesentery, and subsequently disseminate towards the mesenteric lymph nodes [31].

The detection of peritoneal metastases at an early stage could be a key component of effective therapy for diseases spreading abdominal [36, 37]. The main role of tumor cells in FDG uptake had been already pointed out in a study examining peritoneal tumor spread in mice [38].

We believed that the previously well described mouse model could be an optimal model for preclinical investigations dealing with translational detection possibilities of peritoneal spreading. Therefore, we aimed to investigate the early spreading of Bc.DLFL1. lymphoma and compare its detectability in advanced stage, with in vivo FDG-PET and PET/MRI, and ex vivo by autoradiography and CLI using FDG. The results of these imaging techniques were correlated with immunohistochemical tissue analysis.

4 Objectives

In my PhD work, I have used all those imaging methods, which are helpful in the diagnosis and assessment of response to therapy in patients with lymphoma. The dissertation can be divided into a clinical and a preclinical part. Based on the literature, radiomics derived from PET images may contribute to better characterization of tumor in vivo and therefore could help in individualized tumor management. I begin this paper by outlining a related clinical hypothesis. During clinical management, it may occur that the diagnosis is delayed due to an inadequate tissue sampling. In the first preclinical study, we investigated an image-based sampling method using a new and accurate rodent model (spontaneous lymphoma). The spreading mechanisms and routes of lymphoma cells are still unclear. My aim was also to characterise tumour spread and heterogeneity in our rodent experiments both in the first and second part of the preclinical examinations. New diagnostic possibilities emerging from our clinical and preclinical research will be presented based on our published literature.

1. In the clinical study, we deal with the molecular imaging diagnostics of diffuse large B cell lymphoma. In DLBCL despite well-established therapy protocols, 25-30% of patients are resistant to standard chemo-immunotherapy mostly due to heterogeneous origins of the disease. For the identification of high-risk patients in diffuse large B-cell lymphoma we investigated the prognostic significance of in vivo radiomics derived from baseline FDG-PET/CT and clinical parameters utilizing automated machine learning.
2. In the first preclinical study, first we investigated the novel Cerenkov luminescence imaging, which is a promising approach to image-guided surgery and pathological sampling. It could offer additional advantages when combined to whole-body isotope tomographies. We aimed to obtain evidence of its applicability in lymphoma patho-diagnostics, thus we decided to investigate the radiodiagnostic potential of combined PET or SPECT/CLI in an experimental, novel spontaneous high-grade B-cell lymphoma mouse model (Bc.DLFL1).
3. In the second preclinical study we followed the early stage spread of Bc.DLFL1 mouse lymphoma model with different imaging modalities. Thorough our investigations we aimed to confirm the importance of local FDG administration during diagnostic imaging, to precisely assess early peritoneal manifestations.

4.1 The related main targeted points

1. Analysis of a 2-years-event-free prediction model using radiomics derived from pre-treatment FDG-PET/CT of patients with DLBCL

2. Development of a novel imaging tool combining PET/SPECT and CLI to be able to detect the most relevant affected lymph node and/or the most relevant part of the affected lymph node in a mouse model.

3. Select the most optimal nuclear medicine technique for early detection of peritoneal lymphoma spread using a mouse model.

5 Materials and methods:

5.1 Clinical part

The studies involving human participants were reviewed and approved by the appropriate local institutional research ethics committee and the Hungarian National Institute of Pharmacy and Nutrition under permission number 6536 – University of Pécs 2017 and OGYÉI/50268-8/2017. Written informed consent for participation was not required for this study in accordance with the national legislation and the institutional requirements.

5.1.1 Patient's data

The baseline pretreatment FDG-PET/CT scans of 85 patients diagnosed with DLBCL performed in the period between January 2014 and December 2019 were assessed. The FDG-PET/CT scans were carried out in two centers: at University of Pécs, Department of Medical Imaging – Center 1 including 41 patients and at University of Kaposvár, Hungary – Center 2 including 44 patients. The median age of patients in this study population was 59 years (range: 23-81 years) with 48.20% (n: 41) of patients older than 60. In this cohort, 40 (47%) patients were male, and 45 (53%) were female. The patients with incomplete medical records and those who received non-standard treatments were excluded from the final analysis. The Eastern Cooperative Oncology Group (ECOG) performance status >2 was reported in 27 (31.80%) cases (in 2 cases the ECOG status were unknown). All patients were treated with standard R-CHOP-21 treatment regimen for at least 4 full cycles. The patients were classified to germinal center B-cell-like (GCB) or activated B-cell (non-GCB) type using the Hans algorithm [39]. The data regarding the cell of origin (based on Hans algorithm) was available in 82 patients; 29 (37,60%) were GCB, 53 (62,40%) were non-GCB. The clinical-stage was evaluated by modified Ann Arbor and Lugano classification.

The pathological and clinical data, and the Revised International Prognostic Index (R-IPI) were also determined before the initiation of the therapy (R-IPI: 0: 8, 1: 15, 2: 23, 3: 27, 4: 12 patients).

Event-free survival (EFS) was defined as the time from registration date to disease relapse, progression, or death related to the lymphoma. Complete response (CR), partial response (PR), progression (PD), refractory disease, and relapse were defined according to International Working Group response criteria for lymphoma [19, 40].

5.1.2 FDG-PET/CT studies

Pretreatment whole body FDG-PET/CT scans were performed using Mediso AnyScan 16 PET/CT scanner in 41 patients (Center 1) and Siemens Biograph Truepoint 64 PET/CT scanner in 44 patients (Center 2). All patients in the study were subjected to full history and complete clinical examination including the clinical stage of the disease. The patients were instructed to fast for 6 h before the scan. Blood glucose level was ensured to be below <8 mmol/l in all patients before the injection of radiotracer. Intravenous injection (i.v.) of FDG through i.v. line with a dose of 3-4 MBq/kg was administered. After tracer injection, patient was asked to stay for at least 60 minutes in a quite dark room covered by warm blankets. The patients were not allowed speaking, chewing, or reading.

During the PET/CT examination in Center 1, we performed a low-dose CT scan first with the following parameters: X-Ray tube voltage: 120 kVp (depending on the patient's size, 140 kVp is used in bariatric patients), X-Ray tube current: 24–26 mAs (also depending on the patients' size, higher tube current can be applied in bariatric patient), Pitch: 1.5, Slice thickness: 2.5 mm. In order to achieve attenuation correction and accurate body mapping, the CT series has to cover the whole PET range of patients from skull to mid thighs. After this step, the PET acquisition follows the CT series immediately. We have applied 3D acquisition method for PET data collection with 3 minutes frame-time. Usually, general scan range was between 7 to 10 bed positions by Axial FOV:15.12 cm (longitudinal FOV in patient' Z axis). According to manufacturer's recommendations, the PET images were iteratively reconstructed using the Tera-Tomo™ 3D image reconstruction algorithm in a 167x167x234 matrix, which resulted isotropic voxel size of 4mm.

In Center 2, the PET-CT consisted of an initial low-dose CT scan with the following parameters: X-Ray tube voltage: 120kVp (depending on the patient's size, 140kVp is used in bariatric patients), X-Ray tube current: Reference effective mAs:60 using CareDose, Pitch: 1.5, Slice thickness: 5 mm. In order to attenuation correction and accurate body mapping, the CT series shall cover the whole PET range of patients from skull to mid thigs. After this step, the PET acquisition followed the CT series immediately. We applied 3D mode acquisition for PET data collection with 3 minutes frame-time. Usually, general scan range was between 7 to 9 bed positions by Axial FOV:16.2 cm (longitudinal FOV in patient' Z axis). PET images were iteratively reconstructed using 2D OSEM (3i8s, 5 mm Gaussian filtering) image reconstruction algorithm in a 168*168 matrix.

5.1.3 Delineation and Feature extraction

Lymphoma lesions were detected by InterView FUSION ver. 3.10 (Mediso Medical Imaging Systems Ltd, Budapest, Hungary) clinical evaluation software. The average Standardised uptake value – max (SUV-max) value of the liver (3,5-5,5) served as a reference threshold for the semi-automated algorithm [41]. This approach was selected to minimize the effects of patient-specific radiotracer distributions [42]. The average of three randomly placed Volume of interest (VOI) from the unaffected liver regions was used. After the execution of the algorithm with the selected parameters, from the automatically segmented regions, the non-affected regions, such as regions with physiological activity (urine in kidneys or in the bladder, or brain activity) or radiotracer accumulations, which are not related to the lymphoma (such as bowel uptake caused by metformin intake) were manually excluded. Total Lesion Glycolysis (TLG), Total Metabolic Tumor Volume (TMTV), and SUV max were automatically calculated across all delineated lesions. Furthermore SUV-peak values were segmented from the VOI with the highest activity. For further radiomic feature extraction, the largest VOI was selected in each patient. From each of these VOIs, IBSI radiomic features including intensity, histogram, morphological, neighborhood gray-tone difference matrix (NGTDM), gray-level co-occurrence matrix (GLCM), grey level run length matrix, (GLRLM), and grey level size zone matrix (GLSZM) features were extracted. For the IBSI-conform reporting details of the radiomic analysis see (Table 1).

1. Table 1: the Imaging Biomarker Standardization Initiative (IBSI) reporting structure of the study. The information presented herein is based on the IBSI guidelines.

Patient	
Volume of Interest	Predictive value of pretreatment [18F]FDG PET in DLBCL
Patient Preparation	Blood glucose level <8 mmol/l 24 h inactivity and 6 h fasting before tracer administration
Radiotracer	[18F]FDG PET Fluorodeoxyglucose
Acquisition and Reconstruction	
Protocol	Intravenous injection of [18F]FDG 3-4 MBq/kg 60 minutes relaxation after tracer administration No speaking, chewing, or reading was allowed.
Scanner type	Center 1: AnyScan PET/CT (Mediso Medical Imaging Systems) Center 2: Siemens Biograph Truepoint (Siemens)
[18F]FDG PET in Center 1	3D acquisition method Frame time: 3 minutes Bed positions: 7-10 Axial FOV: 15,12 cm Tera-Tomo™ 3D image reconstruction algorithm Matrix: 167x167 Voxel size: 4 mm.
[18F]FDG PET in Center 2	3D acquisition method Frame time: 3 minutes Bed positions: 7-9 Axial FOV:16,2 cm 2D OSEM (3i8s, 5 mm Gaussian filtering) image reconstruction algorithm Matrix: 168x168 Voxel size: 5 mm
CT in Center 1	X-Ray tube voltage: 120kVp (depending on the patient's size, 140kVp is used in bariatric patients), X-Ray tube current: 24–26 mAs (also depending on the patients' size, higher tube current can be applied in bariatric patient). Pitch: 1,5 Slice thickness: 2,5 mm
CT in Center 2	X-Ray tube voltage: 120kVp (depending on the patient's size, 140kVp is used in bariatric patients), X-Ray tube current: Reference effective mAs:60 using CareDose Pitch: 1,5 Slice thickness: 5 mm

Data conversion	
Step 1	BQML voxel units were transformed to weight-normalized SUV automatically by the Interview FUSION software (Mediso).
Segmentation	
Software	Interview FUSION ver 3.10
VOI definition	Standard semi-automated iso-count 3D.
Number of experts	1+1 (1 nuclear medicine expert participated in independent delineations, followed by 1 senior nuclear medicine specialist cross-validation and if necessary, modification of first-round results)
Reference image	PET
Image / VOI interpolation	
Method	Cubic 3D, including nearest 26 neighbors
Grid	Align by center
Extrapolation beyond original image	Neighbor distance search calculated as original voxel size main diagonal + epsilon. Missing value: image minimum
Voxel dimensions	4.0 x 4.0 x 4.0 mm
Partially masked voxels (VOI)	Taken if more than half of original voxel area included
Discretization	
Method	Fixed bin width, variable number of bins
Bin width	0.1 SUV
Image biomarker computation / Parameters	
Intensity features (6): Minimum, Maximum, Mean, Sum, Variance, Local intensity peak **Histogram features** (2): Discretised intensity skewness, (Excess) discretised intensity kurtosis **GLCM features** (4): Joint entropy, Contrast, Inverse difference, Correlation **Morphological features** (2): Volume (mesh), Maximum 3D diameter **GLSZM features** (12): Small zone emphasis, Large zone emphasis, Low grey level zone emphasis, High grey level zone emphasis, Small zone low grey level emphasis, Small zone high grey level emphasis, Large zone low grey level emphasis, Large zone high grey level emphasis, Grey level non-uniformity, Zone size non-uniformity, Zone percentage, Zone size variance **NGTDM features** (3): Coarseness, Busyness, Complexity **GLRLM features** (11): Short runs emphasis, Long runs emphasis, Low grey level run emphasis, High grey level run emphasis, Short run low grey level emphasis, Short run high grey level emphasis, Long run low grey level emphasis, Long run high grey level emphasis, Grey level non-uniformity, Run length non-uniformity, Run percentage	
Software	Interview FUSION ver. 3.10
Distance weighting	No
CM symmetry	Symmetric
CM / ZM distance	Chebyshev distance 1
CM / ZM aggregation	3D, full-merging
Exclusion criteria	VOIs with less than 64 voxels were excluded from the analysis

5.1.4 Reference standard

During the follow up 2-years event free survival were chosen as a clinically relevant cut-off point [8]. Based on this criterion, patients were selected into two groups. In Group 0, the patients had no events during the 2-years follow up, and in group 1 the patients had primary refractory disease or relapsed during the 2-yers period.

5.1.5 Statistical analysis

A chi-squared test was used for the assessment of binary variables via SPSS (SPSS statistical software 27). First, data from both centers were evaluated together based on 2-year event-free survival. A significant association was sought between the two groups, defined above and the following clinical data: sex, stage, R-IPI, COO. Data were also separated by the two centers, where the FDG-PET/CT scans were performed. A significant relationship was sought between the two centers and the two clinical outcomes, stages, R-IPI values and COO. The test results were considered statistically significant if the p-value was under 0.05.

5.1.6 Automated machine learning analysis and biomarker identification

Center 1 dataset was utilized as a training set, given that it had more balanced remission-progression subgroups compared to Center 2 (Table 3). The dataset underwent automated machine learning analysis by the Dedicaid AutoML Research package (Dedicaid GmbH, Vienna, Austria). This step included automated data preprocessing for redundancy reduction, class imbalance reduction as well as feature engineering, ranking and selection [43]. The data was split into 100-folds via random subsampling [44] and mixed ensemble learning was applied in each fold to generate a model predicting final 2-years event free survival. For quality control, the AutoML approach also performed a single-center cross-validation across the 100-folds of Center 1. Lastly, the final feature ranking was generated by averaging the 100-fold feature importance and normalizing them to the sum of 1.0. Features higher than half of the highest feature rank were considered high-ranking and were analyzed for imaging biomarker identifications.

5.1.7 Independent validation of prediction model

The dataset of Center 2 was utilized to as independent test set to validate the established predictive model built by the dataset of Center 1. Confusion matrix analytics were utilized to

calculate the number of true positive, true negative, false positive and false negative prediction occurrences of each Center 2 case. Sensitivity, specificity, positive predictive value, accuracy, and area under the receiver operator characteristics curve (AUC) were calculated across the validation cases.

5.2 Preclinical studies 1

The study was approved by the Local Ethics Committee of the University of Pécs. Furthermore, all procedures involving live animals were carried under permission of the National Food Chain Safety Office of Hungary, Department of Animal Health, under license number BA02/2000-16/2015.

5.2.1 Experimental animal model of Bc.DLFL1 lymphoma propagation

All studies reported here have been carried out in accordance with the rules on animal welfare and regulations on other respective subjects in vigour in Hungary. The study had been designed and performed in compliance with the ARRIVE guidelines. BALB/c mice bred at the SPF Animal Breeding Unit of the University of Pécs, Department of Immunology and Biotechnology, aged between 8-12 weeks, were used as lymphoma recipients. After retrieval, the mice were adapted to conventional animal facility of the Department of Immunology and Biotechnology. The Bc.DLFL1 lymphoma cells were maintained as serial intraperitoneal passage.

5.2.2 Grouping and number of animals by tumor stage

In both the FDG-PET and the ^{67}Ga-citrate SPECT/MRI experiments animals were grouped into early stage (imaging 4 days post inoculation of lymphoma cells), advanced stage (imaging 8 and 9 days post inoculation) and terminal stage (imaging 11 and 12 days post inoculation). (Altogether 36 mice at inoculation were grouped into six groups with six mice per group.) Each stage groups contained n=6 animals per radiopharmaceutical. However, in the end-stage DLBCL group of animals at 11 days post inoculation, deaths occurred thus five animals were amenable to the combined in vivo tomographic - ex vivo CLI imaging from the FDG-PET group, and one animal was usable for the ^{67}Ga-citrate SPECT/MRI imaging from its group of originally six animals.

5.2.3 In vivo imaging using FDG PET/MRI

Each animal received between 10-15 MBq of FDG (Pozitron-Scan, Pozitron, Hungary) i.v. in a 0.1 mL lateral tail vein injection 1 hour before the PET and 1.5 hours before the subsequent CLI imaging. Animals were fasted for 8 hours before scans. PET and MRI images were acquired in a nanoScan 1 Tesla PET/MRI system (Mediso Ltd, Hungary) and in a Micropet P4 (Concorde Microsystems, US) small animal PET system. Static scans of 15-minute duration were collected 60 minutes post injection in an energy window of 350-750 keV. All PET images were reconstructed using the respective device`s three-dimensional Maximum A Posteriori (MAP, P4 system) or three-dimensional Monte-Carlo modeled Ordered Subsets Expectation Maximisation (Tera-Tomo 3D-OSEM, Mediso system) algorithm, with corrections for dead time, scatter, and attenuation where available. Reconstructed images of 1 mm voxel size were then visualised using the VivoQuant (inviCRO, USA) and Fusion (Mediso, Hungary) softwares. All MR images were acquired in a Mediso nanoScan 1T MRI with a three-dimensional T1-weighted gradient echo sequence, with 300 micron voxel size, 6 excitations, 12.1 ms/ 2.9 ms Transmit/Receive times, and 15 degrees of flip angle.

5.2.4 In vivo imaging using ^{67}Ga-citrate SPECT/MRI

For SPECT, 4.1-5.4 MBq of ^{67}Ga-citrate (CIS Bio, France) was injected iv. in 0.2 mL 24 hours before imaging A 45-minute SPECT scan was then performed using a NanoSPECT/CT Silver Upgrade small animal SPECT system (Mediso Ltd, Hungary) using both the 93 keV and 184 keV photopeaks in a 20%-20% energy window, with 60 acquisition views and a Monte-Carlo model based three-dimensional SPECT reconstruction (Tera-Tomo, Mediso Ltd, Hungary) resulting in an image volume of 0.6 mm voxels. The same animal in the same animal bed allowing constant position was then immediately subjected to a whole-body three-dimensional MR imaging sequence in the nanoScan 1T MRI subcomponent. After these acquisitions, tissues were examined with ex vivo CLI, histology and immunohistochemistry following the in vivo imaging. All live animal image acquisitions were performed under 2% isoflurane anesthesia in medical oxygen in a special cross-compatible animal holder bed (MultiCell, Mediso, Hungary) which kept the animals immobilised during cross-modality and cross-device scans.

5.2.5 Processing of ex vivo tissues for CLI and subsequent histology in situ

The entire gastrointestinal tract (between the subphrenic segment of oesophagus and the upper third of rectum together with the adjoining mesentery) was removed and placed in a 10 cm Petri dish, with the intestinal folds flattened. Under gentle pressure the dissected gut-

mesentery complex was fixed in cold 4% buffered paraformaldehyde for 15 minutes, followed by repeated rinsing with PBS. The entire complex was stained with Mayer's hematoxylin solution for 10 minutes, followed by blue stain intensification in tap water for 5 minutes.

5.2.6 CLI Imaging

Following the end of PET acquisitions, Cerenkov light imaging of the Cerenkov luminescence produced in the tissues containing high concentrations of the injected radionuclidic tracer, was performed using a prototype high resolution Cerenkov imaging system with an exceptionally sensitive imaging chain. (LighPath, Lightpoint Medical, UK) Tissue specimens were placed in the sample holder of the instrument and image acquisition was performed over them for 10 minutes of signal integration, with 4x4 pixel binning in 512x512 pixels, with a 0.15 mm pixel size of the imaging chain in a field of view of 8x8cm. White light photographic background was also collected by the instrument for anatomical reference. Images of Cerenkov Luminescence and the background white-light images were exported to DICOM format by the instrument`s dedicated software. Further two-dimensional rigid co-registration, post-processing with a median filter of 3 pixels kernel, rotation and color look-up table changes were done using Fusion (Mediso, Hungary) and VivoQuant (inviCRO, USA). Images were then visualized with a unified common colour Look-Up Table (LUT) across animals, with arbitrary units of light intensity based on the emCCD detector pixel counts overlaid on the white-light photographs.

The clinical prototype LightPath system used in the study had, under the same detector pixel binning condintions as mentioned above, a minimum detectable activity of 20 kBq in a scan time of 100 s and a volume of 0.02 mL for ^{18}F in a 0.315 mm radius microwell. During the evaluation of system performance for setting up the ^{67}Ga study, we measured a minimum detectable activity of 300 kBq of ^{67}Ga isotope, in an equivalent scan time for a similar well, volume of 0.02 mL with the same resolution.

5.2.7 Histology and immunofluorescence

Those lymph nodes that have been identified as tumorous, and all spleens, were processed for haematoxylin-eosin (H&E) histology. They were fixed in 10% buffered formaldehyde using standard histological protocols. Immunofluorescence for lymphoma identification was performed with cryostat sections from tissue blocks embedded in OCT medium (BioOptica, Italy) using FITC-conjugated rat anti-mouse IgM (clone B7.6) and Alexa Fluor 647-conjugated rat anti-mouse B220 (clone RA3-6B2) monoclonal antibodies produced

at the Department of Immunology and Biotechnology, University of Pécs. The sections were and analysed using BX61 Olympus microscope using the AnaliSys software.

5.2.8 Flow cytometry

Mesenteric lymph nodes of lymphoma-bearing mice were collected and crushed between two frosted ends of histological glass slides. The cells were filtered through 70 μm cell strainers and centrifuged. After resuspension in PBS-0.1% BSA-0.1% Na-azide buffer, the cells were incubated with FITC-conjugated anti-mouse IgM and Alexa Fluor 647-conjugated anti-B220 mAbs. Lymphoma cells and residual lymphocytes were distinguished by gating on forward and side scatter (FSC/SSC) parameters related to size and granularity, respectively, using a BD FACSCalibur flow cytometer and CellQuest Pro software (both BD Biosciences, UK).

5.3 Preclinical studies 2

5.3.1 FDG uptake test of Bc.DLFL1 mouse lymphoma cells in vitro:

Mesenteric lymph nodes of two lymphoma-bearing and two healthy BALB/c mice were collected and homogenized. The homogenates were filtered through 70 μm cell strainers and centrifuged. The cells were counted in a Bürker chamber and the preparation was diluted to the desired cell density. We compared the FDG uptake of 107/ ml lymphoma cells to that of 107/ ml mixed lymphocytes from healthy animals. Two comparative measurements (Hidex Triathler, Hidex, UK) were performed under the same conditions in triplicates. The mixed leukocyte cells were then subjected to the same incubation procedure as the lymphoma cells (see below). The freshly isolated cells were maintained in physiological saline for 1 hour and then centrifuged (5,000 g for 5 minutes) at 37oC. At the same temperature, 1 ml of FDG solution in physiological saline with a radioactivity of 100 kBq was added to the cell pellet and was thoroughly mixed. After 1 hour of incubation time for tracer uptake, the cells were centrifuged, the fluids (supernatant-1) were removed and their activity measured. After re-suspension and repeated centrifugation, the second set of fluids (supernatant-2) was removed and the activities of both cell pellet and supernatant-2 were measured. The distribution ratio of FDG between the cell pellet and the sum of supernatants-1 and -2 was calculated.

5.3.2 Experimental animals and Bc-DLFL.1 lymphoma propagation

BALB/c mice were used as lymphoma recipients aged between 8-12 weeks were bred at the SPF Animal Breeding Unit, and after retrieval, the mice were adopted to conventional animal

facility of the Department of Immunology and Biotechnology. The Bc.DLFL1 lymphoma cells were maintained as serial intraperitoneal passage in mice.

$5x10^6$/ml lymphoma cells in DMEM tissue culture medium (Sigma-Aldrich) were incubated in 5µM 5-6-carboxyfluorescein succinimidyl ester (CFSE) dissolved in DMSO at 37ºC for 20 minutes as previously described [39]. After washing in DMEM containing 10% foetal bovine serum the cells were adjusted to 10^6 cells/recipient in 0.5ml, and were injected intraperitoneally.

Mice were grouped into an early stage group where imaging was performed one day post inoculation of lymphoma cells (n=18 mice), and into an advanced stage group with imaging of n=3 mice performed 7 days post inoculation of the cells.

In the early stage group, nine animals received intraperitoneal injection of FDG and equally, nine mice received FDG via the intravenous administration route in the lateral tail vein. The advanced stage group received intravenous FDG injections.

5.3.3 In vivo imaging using FDG-PET

Each animal received between 10-15 MBq FDG (Pozitron-Scan®, Pozitron, Hungary) in 0.1 mL injection 1 hour before the PET and 1.5 hours before the subsequent CLI imaging. Animals were fasted for 8 hours before scans. PET were acquired in a Micropet P4 (Concorde Microsystems, US) small animal PET system. Static scans of 15-minute duration were collected 90 minutes post injection in an energy window of 350-750 keV. All PET images were reconstructed using device`s three-dimensional Maximum A Posteriori (MAP, P4 system) algorithm, with corrections for scatter, and attenuation where available. Reconstructed images of 1 mm voxel size were then visualised using the VivoQuant (inviCRO,USA) and Fusion (Mediso, Hungary) softwares.

5.3.4 In vivo imaging using PET/MRI

Mouse PET/MRI measurements were performed in a MultiCell™ heating, positioning and monitoring multi-animal bed on an nanoScan 1T integrated imaging systems (both Mediso Ltd, Budapest, Hungary). Ninety minutes after FDG injection, a 15-minute static PET data acquisition was obtained in an energy window of 350-750 keV, immediately followed by a three-dimensional T1-weighted gradient echo sequence, with 300 micron voxel size, 6 excitations, 12.1 ms/ 2.9 ms Transmit/Receive times, and 15 degrees of flip angle.Quantitative radioactivity PET data were reconstructed using a Monte-Carlo based iterative algorithm (Tera-

Tomo™, Mediso Ltd, Budapest, Hungary) using the MRI as anatomical and attenuation priors, with 0.3 mm voxel size for a whole-body PET/MRI image with a resolution of 1 mm.

5.3.5 Processing of ex vivo tissues for autoradiography and CLI

24 hours or seven days (for the advanced stage group) after the lymphoma inoculation, and after the PET acquisition the entire gastrointestinal tract (between the subphrenic segment of oesophagus and the upper third of rectum together with the adjoining mesentery) was removed and placed in a 10 cm Petri dish, with the intestinal folds flattened. Under gentle pressure the dissected gut-mesentery complex was fixed in cold 4% buffered paraformaldehyde for 15 minutes, followed by repeated rinsing with PBS.

5.3.6 Autoradiography

Phosphor imager plate autoradiography (ARG) was performed on the fixated gastrointestinal tract preparations 2 hours post harvesting the organs. A GE Typhoon 9400 (General Electric, USA) imager was used with the sections incubated for 10 minutes on the plates, with 100 micron voxel size and the dedicated image export function was applied to obtain tiff format high-resolution images that were in turn visualized further with either ImageJ or VivoQuant softwares.

5.3.7 Cerenkov Light Imaging ex vivo

Following the end of PET acquisitions, Cerenkov light imaging of the Cerenkov luminescence produced in the water of tissues with high concentration of the injected radionuclidic tracer, was performed using a prototype high resolution Cerenkov im-aging system with an exceptionally sensitive lens. (LighPathTM, Lightpoint Medical, UK) Tissue specimens were placed in the sample holder of the instrument and image acquisition was performed over them for 10 minutes of signal integration, with 4x4 pixel binning in 512x512 pixels, with a 0.1 mm pixel size. Black and white light photographic background was also collected by the instrument for anatomical reference. Images of Cerenkov Luminescence and the background white-light images were exported to DICOM format by the instrument`s dedicated software. Further two-dimensional rigid co-registration, post-processing with a median filter of 3 pixels kernel, rotation and color look-up table changes were done using Fusion (Mediso, Hungary) and VivoQuant (inviCRO, USA). Images were then visualized with a unified common colour Look-Up Table (LUT) across animals, with arbitrary units of light intensity based on the emCCD detector pixel counts overlaid on the black-and-white photographs.

5.3.8 Fiber-optic confocal endomicroscopy imaging of FITC molecules ex vivo

Thereafter, the S1500 fiberoptic microscope probe tip (resolution 3.3 microns, field-of-view diameter, 600 microns) of the Cellvizio Lab Dual Band imaging system (Mauna Kea Technologies Inc, Paris, France) was applied onto the lymph nodes and 480 nm green bandwidth live microscopic images of the intestinal walls, peritoneal surfaces and lymph nodes or visible lympatic vessels were collected. Using this method, individual tumor cells can be visualized by their FITC fluorescent dye content in the ex vivo intestinal organ preparations. The imaging was performed immediately post autopsy of the animals.

5.3.9 Immunohistochemistry

The CFSE-labeled lymphoma cells were detected using anti-FITC immunohisto-chemistry. First the gut-mesentery complex previously fixed in 4% buffered paraform-aldehyde for 30 minutes was extensively washed in PBS, and then incubated with 1 mg/ml phenyl-hydrazine hydrochloride (Sigma-Aldrich) in PBS to block endogenous peroxidase activity, followed by saturation in 5% BSA-PBS-0,1% saponin for two hours at 4ºC with continuous shaking. HRP-conjugated sheep anti-fluorescein antibody (Southern Biotech) diluted in 0,1% BSA-PBS-0,1% saponin was added and incubated overnight with continuous shaking. After extensive washing in PBS-0,1% saponin, the immune reaction was visualized using DAKO diamino-benzidine/H_2O_2 substrate in 5 mM TRIS buffer, pH:7.2.

The immunohistochemical staining for Ki-67 and B220 antigens was performed as previously described [31].

Lymphoma-infiltrated mesentery and mLNs were embedded in Killik freezing medium and frozen. Frozen sections at the thickness of 8µm were cut using a Leica cryostat and were allowed to dry overnight. After fixing in cold acetone for 5 minutes, the sections were dried, followed by rehydration in 1 mg/ml phenyl-hydrazine-PBS solution for 20 minutes. Anti-Ki-67 rat mAb (clone #11F6 from Biolegend [Biomedica Hungaria Kft], Budapest, Hungary, at 1:100 dilution in PBS) or anti-B220 hybridoma supernatant (clone #RA3-6B2) for 45 minutes, followed by washing. Next the sections were incubated with ImmPRESS goat anti-rat IgG-HRP polymeric conjugate (Vector Laboratories, BioMarker, Gödöllő, Hungary) for 45 minutes, and after washing the rections were visualized using DAKO diamino-benzidine/H_2O_2 substrate in 5 mM TRIS buffer, pH:7.2.

6 RESULTS

6.1 Clinical part

In DLBCL patients, disease characteristics and outcomes vary widely, pointing to the importance of patient's classification through identification of sensitive prognostic features especially prior to the start of therapy. For this purpose, we have tried to elucidate the prognostic significance of metabolic heterogeneity [45]. We have highlighted metabolically active tumor volume and standardized uptake value -based parameters such as SUV-max, SUV-min, TMTV, and TLG and compared their applicability with other radiomic parameters as well as clinical and pathological data.

We hypothesize that two-year event-free survival prediction models built on these features is feasible by utilizing automated machine learning in a multi-center environment. Hence, the objectives of this study were: (a) to collect a dual-center dataset including conventional PET, radiomics and clinical parameters of DLBCL patients; (b) to build a two-year event-free survival prediction model by using one center data and (c), to validate the established model by an independent dataset coming from another center.

6.1.1 Patient data

At the end of the standard induction therapy, 55 patients achieved complete metabolic remission. During the 2-year follow-up, 14 patients had primary refractory disease, 14 patients relapsed within 12 months, and 2 patients had relapsed between 12 and 24 months. In summary, after the end of therapy, 30 patients had detectable metabolically active tumor tissue and relapsed within 24 months (Figure 3).

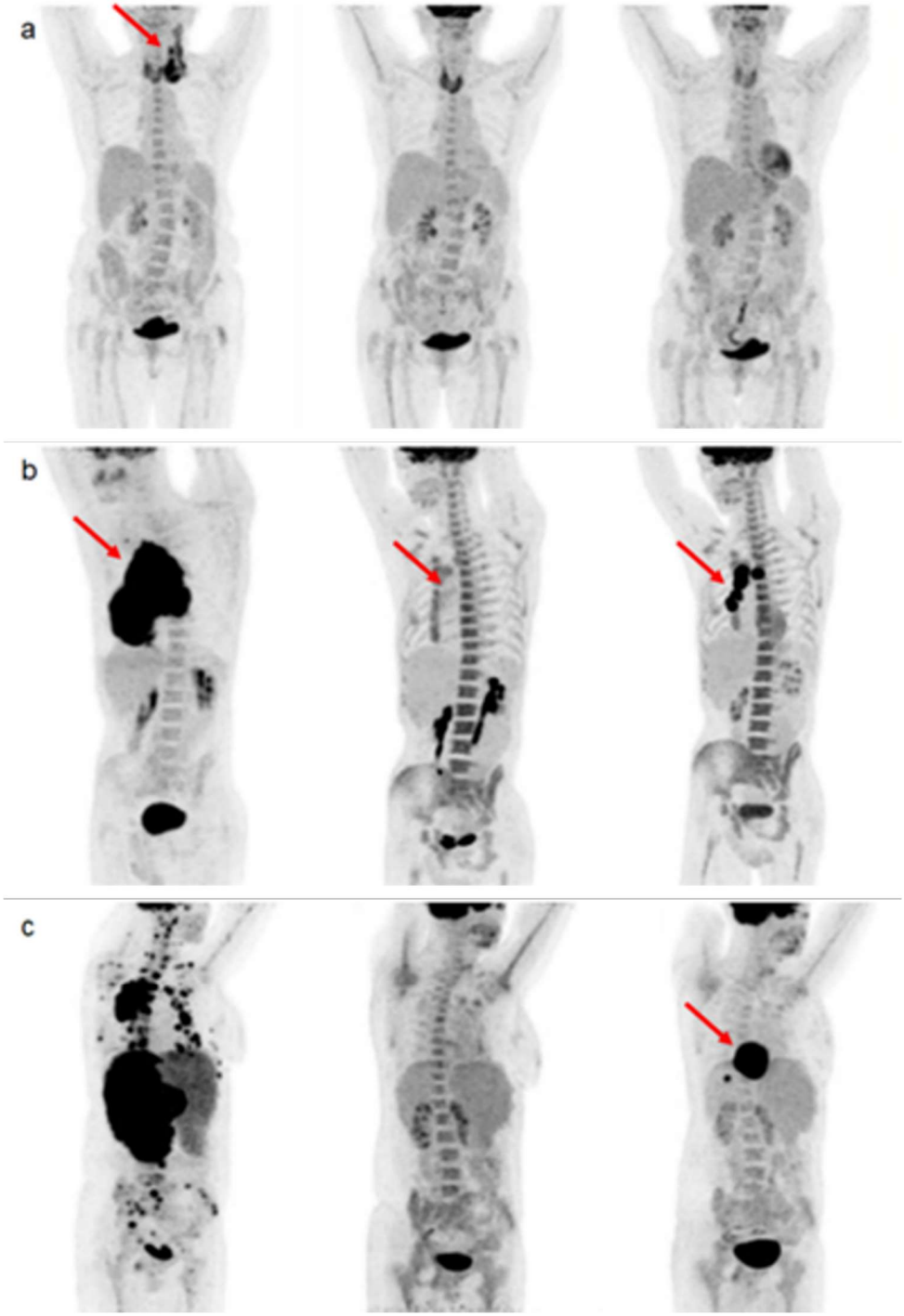

3. Figure 3: Comparison of clinical outcomes based on maximum intensity projection (MIP) images in three patients (a-c). By each patient, the first image shows primary staging, the second shows interim PET scan, and the third shows post-treatment restaging scan. The red arrows indicate FDG avid lymphoma foci. (a): Patient in complete remission to treatment. The increased FDG uptake in all three images were a sign of thyroiditis. (b): Patient without complete remission during, and after the therapy. The interim scan showed Deauville score 4. (c): Patient had an interim scan with Deauville score 3 but relapsed after the treatment.

6.1.2 Statistical analysis

Using the data of Chi-square test, a significant association between Cell of Origin (COO), R-IPI, or stages and previously described two specific groups (0 or 1) was identified. There were significantly more patients in group 1 with non-GCB subtype, who had higher R-IPI values and stages. No significant difference was detected between the patients' sex and the specific groups. The clinicopathological features of patients are described in (Table 2).

2. Table 2: Comparison of clinical outcome of the patients and their clinical data. Chi square test were performed in order to find association between the outcome and the specified clinical status of the patients suffering in DLBCL.

Variables	**No Progression or Remission**	**Progression within 24 months**	**p-value**
Sex, n=85	**(n=55)**	**(n=30)**	
Male (n, %)	28 (32.9%)	17 (20%)	**0.611**
Female (n, %)	27 (31.8%)	13 (15.3%)	
ECOG, n=83	**(n=55)**	**(n=28)**	
0 (n, %)	16 (19.3%)	6 (7.2%)	
1 (n, %)	26 (31.3%)	8 (9.6%)	**0.113**
2 (n, %)	11 (13.3%)	12 (14.5%)	
3 (n, %)	2 (2.4%)	2 (2.4%)	
Stage, n=85	**(n=55)**	**(n=30)**	
1 (n, %)	10 (11.8%)	0	
2 (n, %)	17 (20%)	5 (5.9%)	**0.017**
3 (n, %)	9 (10.6%)	8 (9.4%)	
4 (n, %)	19 (22.6%)	17 (20%)	
R-IPI, n=85	**(n=55)**	**(n=30)**	
0 (n, %)	7 (8.2%)	1 (1.2%)	
1 (n, %)	29 (34.1%)	9 (10.6%)	**0.015**
2 (n, %)	19 (22.6%)	20 (23.5%)	
COO, n=82	**(n=53)**	**(n=29)**	
GC (n, %)	27 (32.9%)	7 (8.5%)	**0,018**
N-GC (n, %)	26 (31.7%)	22 (26.8%)	

In addition, patients were divided on the basis of the center where FDG-PET/CT scan was performed. No association between the above specified two clinical outcomes (based on 2 years event-free survival), R-IPI, stages, or COO and the center where the examinations were performed were identified (Table 3).

3. Table 3: Comparison of patients regarding to the two clinical centers where the FDG PET/CT examinations were performed.

Variables	**Center 1 (Pécs) (n=41)**	**Center 2 (Kaposvár) (n=44)**	**p-value**
Clinical outcome, n=85			
No Progression or Remission (n, %)	25 (29.4%)	30 (35.3%)	***0.487***
Progression within 24 months (n, %)	16 (18.8%)	14 (16.5%)	
Lymphoma stage, n=85			
1 (n, %)	6 (7%)	4 (4.7%)	
2 (n, %)	11 (12.9%)	11 (12.9%)	**0.877**
3 (n, %)	10 (11.8%)	7 (8.2%)	
4 (n, %)	14 (16.5%)	22 (25.9%)	
R-IPI, n=85			
0 (n, %)	4 (4.7%)	4 (4.7%)	
1 (n, %)	18 (21.2%)	20 (23.5%)	**0.988**
2 (n, %)	19 (22.6%)	20 (23.5%)	
COO, n=82	**(n=41)**	**(n=41)**	
GC (n, %)	18 (22%)	16 (19.5%)	**0.654**
N-GC (n, %)	23 (28%)	25 (30.5%)	

6.1.3 Automated machine learning analysis and biomarker identification

Automated machine learning yielded 66% sensitivity, 77% specificity, 78% positive predictive value, 70% negative predictive value, 71% accuracy and 0.74 AUC single-center cross-validation performance in Center 1.

Feature ranking revealed that the most important features for building 2-years event free survival prediction are: max diameter (9%), NGTDM busyness (9%), TLG (8%), TMTV (8%) and NGTDM Coarseness (5%). The distributions of these parameters are plotted on violin plots (Figure 4).

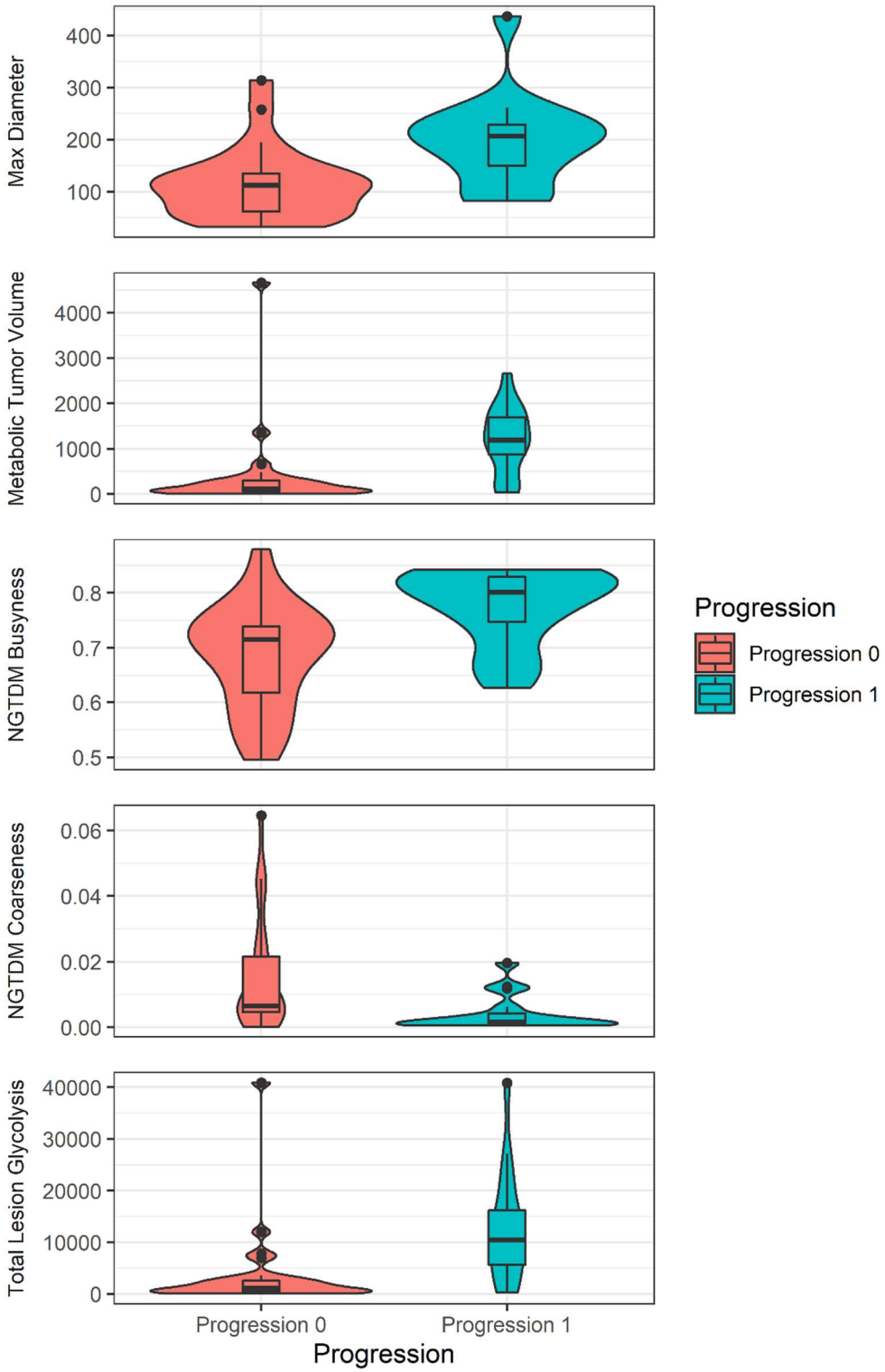

4. Figure 4: The Violin plot (R: A Language and Environment for Statistical Computing, version 4.04., using package ggplot2, version 3.3.3) shows the values of the prominent features to predict 2-year event-free survival.

6.1.4 Independent validation of prediction model

The predictive model built on Center 1 dataset yielded 79% sensitivity, 83% specificity, 69% positive predictive value, 89% negative predictive value, 82% accuracy and 0.85 AUC by evaluating the Center 2 dataset. See Figure 5 for the Receiver Operator Characteristics Curve (ROC) of the independent validation performance over Center 2 cases. See Figure 6 for the Kaplan-Meier curve of the machine learning prediction vs. event-free survival over samples of Center 2.

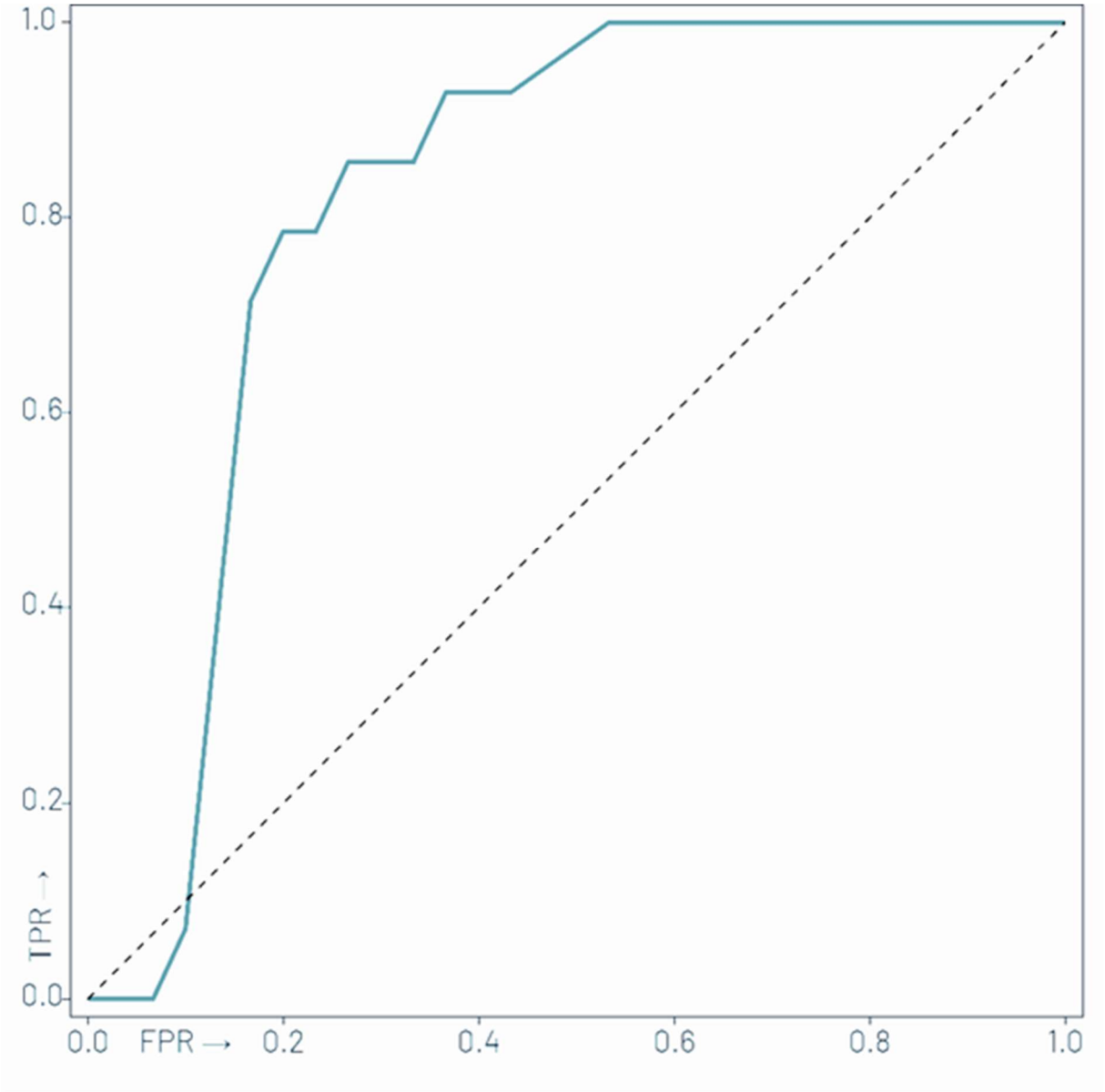

5. Figure 5: Receiver Operator Characteristics Curve (ROC) of the independent validation performance of the machine learning model trained over Center 1 cases to predict 2-year event-free survival over Center 2 cases with Area Under the ROC (AUC) of 0.85.

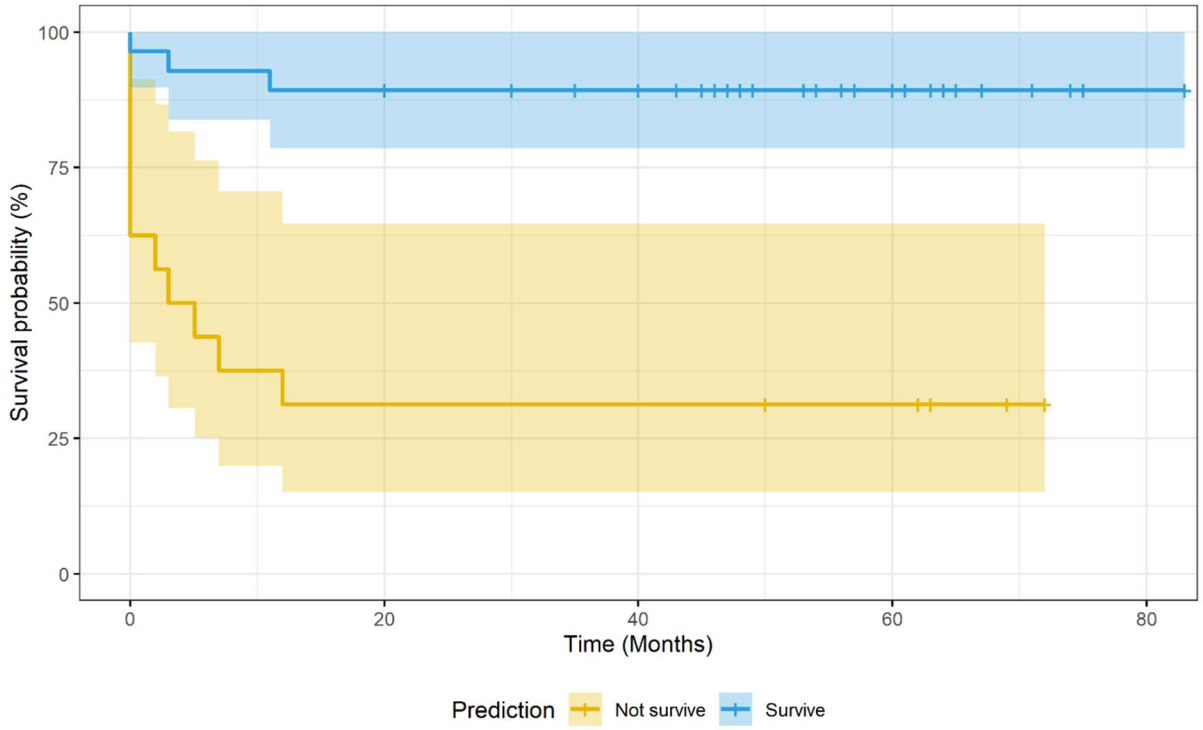

6. Figure 6: Kaplan-Meier curve of the machine learning (ML) model prediction vs. 2-year event-free survival in Center 2 cases. The ML model was trained with Center 1 cases.

6.2 Preclinical studies 1: focus on CLI imaging

We assessed CLI combined with the usual FDG-PET/MRI and ^{67}Ga-citrate SPECT/MRI imaging, too. We also investigated whether the use of a CLI device could help to monitor the spreading of the DLBCL model *ex vivo* and if this CLI device could detect details of metastatic foci. Animals were imaged in three tumor stages for both radiopharmaceuticals: at an early stage of 4 days post inoculation, in the advanced stage at 8 days and in terminal stage. CLI was aimed to direct the search for small or heterogeneous tumorous foci. Using this imaging sequence, the presented methodology of tailored ex vivo selection and histopathologic processing of tumor volumes can also progress towards clinical translation.

6.2.1 Early stage DLBCL escapes radioisotopic whole-body and tissue-level detection with PET, SPECT or CLI

Every animal in each group of the early stage FDG group and also in the early (4 days post inoculation) and advanced stage ^{67}Ga-citrate group could be tested for signal capture and levels in tomographic in vivo and Cerenkov Light imaging. No circumscribed tumor uptake was seen over the background with either FDG or ^{67}Ga-citrate in early stage animals (n=3 for

FDG, n=3 for ^{67}Ga-citrate). Using ^{67}Ga-citrate, no clearly distinguishable SPECT foci nor visibly tumor-associated Cerenkov signal was seen in advanced-stage animals either.
^{67}Ga-citrate SPECT and subsequently ^{67}Ga-citrate CLI detected lymphoma only at its terminal, very advanced stage. However, a well identifiable ^{67}Ga-Cerenkov light signal was captured in the physiologically Gallium-avid regions of the mouse intestines in all imaged animals regardless of tumor stages. In the case of the advanced (8 days post inoculation) stage lymphoma SPECT and CLI images with ^{67}Ga-citrate, high background bowel activity and consequent CLI signal hampered the distinguishing of tumor signal from background CLI luminescence of ^{67}Ga in mesenteric and abdominal scans, thus interpretation of images to tumorous or non-tumorous uptake was not possible (data not shown).

6.2.2 Characterization of FDG uptake is feasible both in vivo with PET/MRI and ex vivo with CLI in advanced stage lymphoma

Using in vivo PET/MRI we found that in an advanced lymphoma stage (at or beyond day 8 post-injection) the infiltrated mesenteric lymph nodes clearly showed a significant accumulation of FDG following intravenous administration (Fig. 7). With CLI we observed FDG accumulation in the infiltrated adipose tissue along the mesenteric vessels, within the enlarged mesenteric lymph nodes, in the omentum and also in the splenic hilus. Subsequent histological analysis of the FDG signal-positive regions confirmed large infiltrates of lymphoma cells at these sites (Fig. 8). For the quantitative assessment of the degree of lymphoma infiltration, flow cytometric analysis was performed. Lymphoma cells could be distinguished using forward and side scatter (FSC/SSC) parameters reflecting size/granularity characteristics, with the lymphoma cells displaying substantially larger size. However, even at the advanced stage of lymphoma, some residual lymphocytes within the affected mesenteric lymph nodes could still be detected, including both CD3-positive T cells and B220-positive normal B cells, latter population also displaying surface IgM. On the other hand, the infiltrating lymphoma cells express only B220, confirming their DLBCL characteristics (Fig. 9).

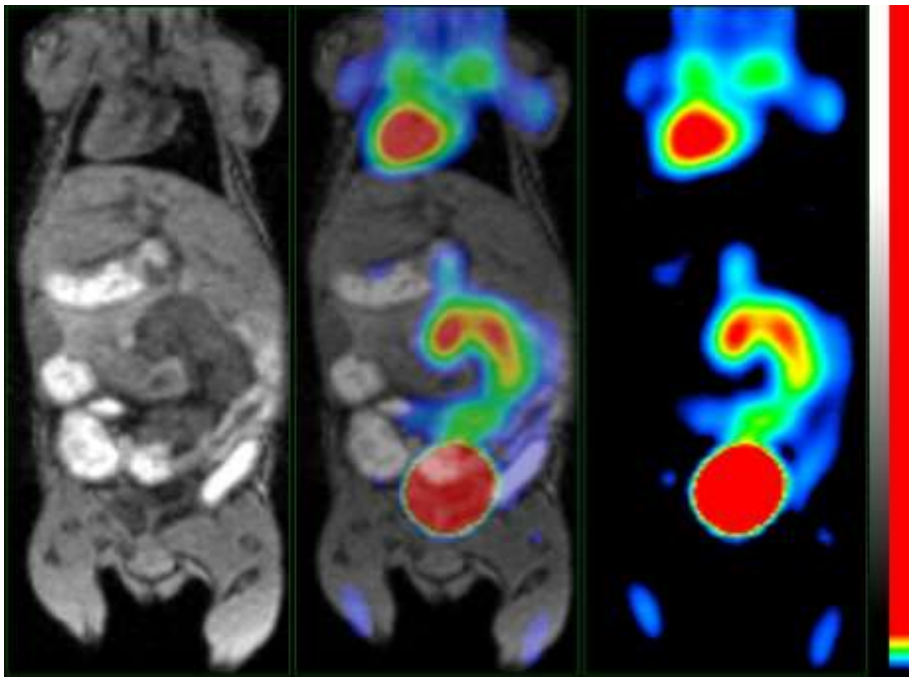

7. Figure 7: Molecular imaging results in advanced stage lymphoma-bearing mice: PET/MR image in advanced stage: FDG-avid enlarged mesenteric lymph nodes are visible (horizontal plane, representative image).

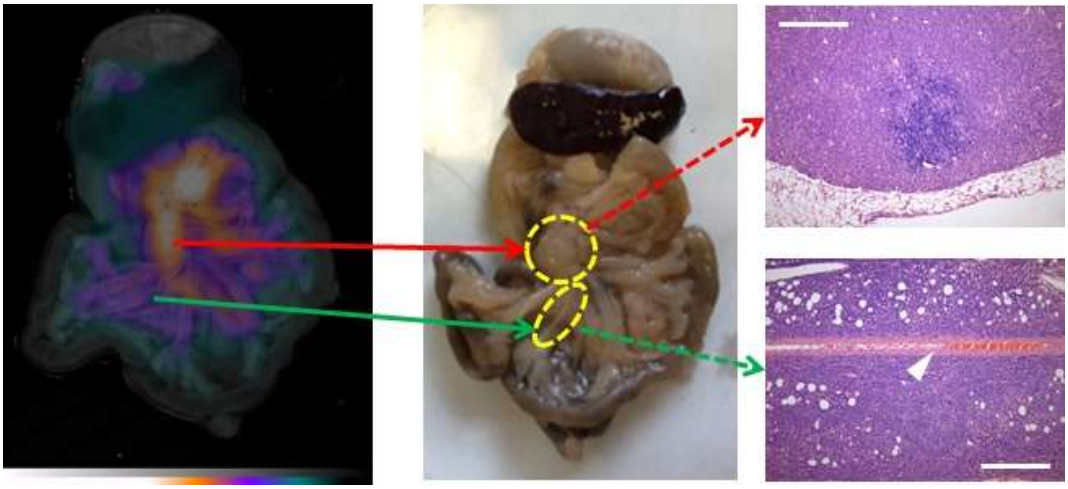

8. Figure 8: Ex-vivo CLI in late stage lymphoma: FDG-avid Bc-DLFL.1 lymphoma foci with H&E staining in mesenteric lymph node (top) and mesenterium (bottom) CLI (left) and, Stereomicroscopic picture of the intestinal preparation (middle), Histology (right): the red arrow shows that the upper encircled area in the stereomicroscopic picture emits Cerenkov light and corresponds to the mesenteric lymph node complex, containing a massive lymphoma infiltrate demonstrated on the top right image (connected by dashed red arrow). The bottom green arrow connects one branch of the mesentery with lesser Cerenkov signal intensity (marked with ellipse), with an extensive lymphoma infiltrate surrounding the mesenteric artery (arrowhead). Scale bar = 200 μm.

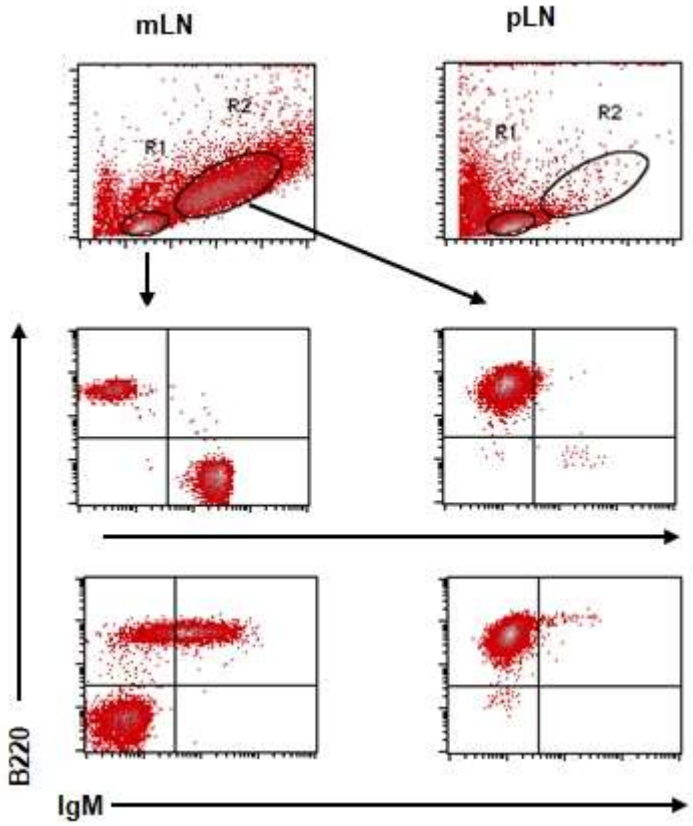

9. Figure 9: Flow cytometric analysis of enlarged mesenteric lymph nodes (mLN) reveals residual small-sized (in R1 gate) CD3-positive T cells and B220-positive B cells (left, middle), latter cells mostly co-expressing IgM (left, bottom), and large number of blast-sized cells (in R2 gate) displaying B220 B-cell marker and absence of CD3-positive cells (right, middle), but lacking surface IgM and CD3 (right, bottom). Lymphocytes from peripheral lymph nodes (pLN) do not contain a distinguishable blast population within the R2 gate (right, top).

6.2.3 Ex vivo CLI discerns tumorous infiltrate within lymph nodes identified as distant metastases using ^{67}Ga-citrate SPECT/MR

At the advanced stage, the enlarged mesenteric lymph nodes (Fig. 10a) are well detectable using MRI. The distinction of ^{67}Ga-citrate accumulation signals in the lymph nodes based on the SPECT alone without MRI would be difficult due to the high background activity caused by the intense non-specific intestinal accumulation of the tracer. On the other hand, the mediastinal region lacks this background. This allows specific detection of distant manifestations with SPECT, even in tissues without obvious MR alterations. Here the SPECT assessment could clearly reveal lymphoma accumulation in the region of parathymic lymph nodes, which were not well noticeable using only MRI analysis in the end-stage lymphoma-bearing mouse (Fig. 10b). The presence of lymphoma infiltrate in parathymic lymph nodes was

verified following their removal by using ex vivo CLI (Fig. 10c) and subsequent histological analysis, including dual immunofluorescence labelling for IgM and B220. This approach allows the identification of lymphoma cells by the lack of surface IgM and the preserved expression of B220 marker, thus distinguishing the lymphoma cells from the B220+/IgM+ normal B cells (Fig. 10 d, e, f).

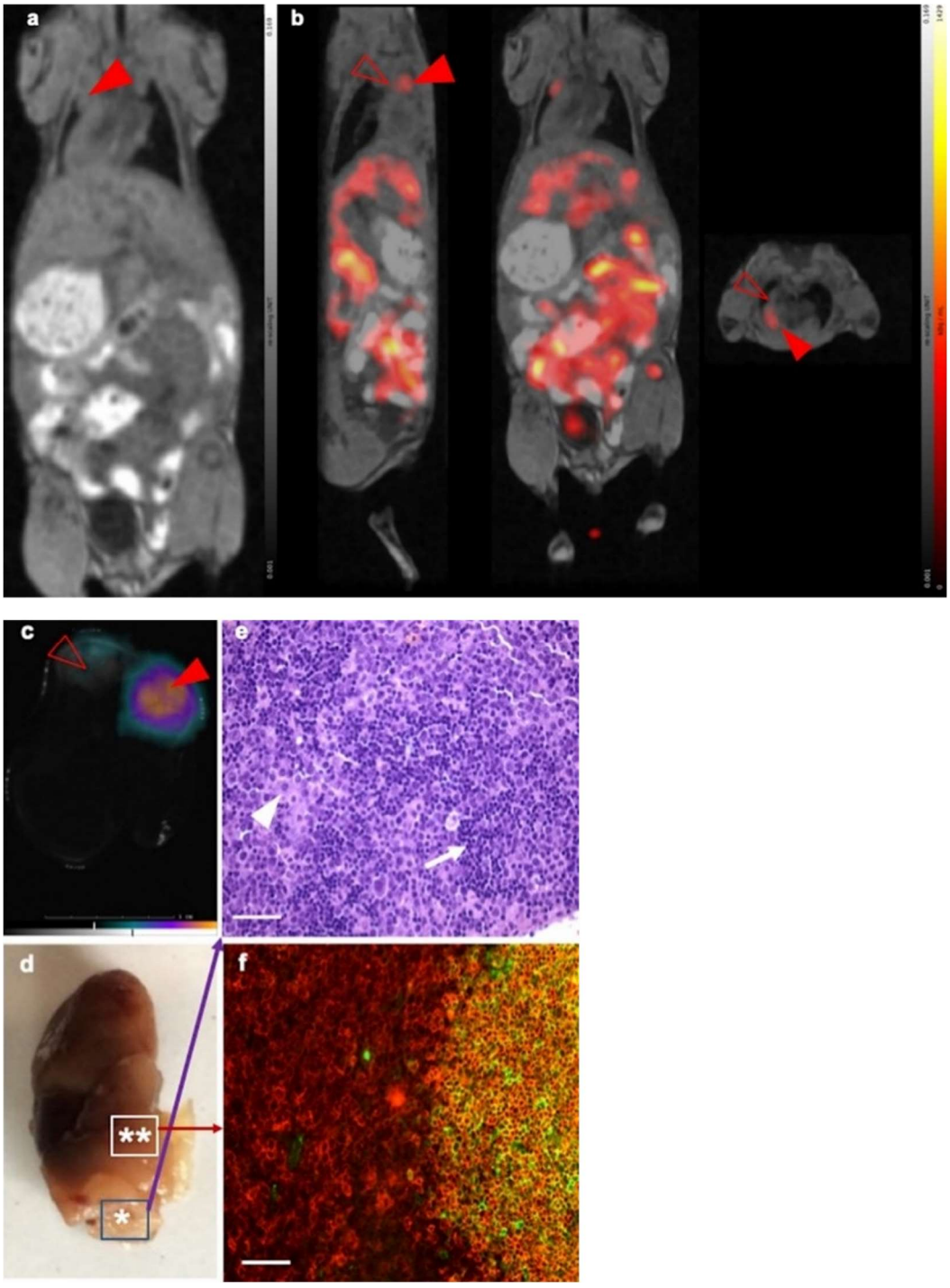

10. Figure 10: End-stage lymphoma-bearing mouse images show specific accumulation of ^{67}Ga-citrate in parathymic lymph nodes. (a) MRI: enlarged mediastinal lymph node conglomerate with signs of

tumor infiltration (red arrowhead). (b) ^{67}Ga-citrate SPECT/MRI: SPECT/MRI assessment shows tracer accumulation in a part of the left parathymic lymph node (from left to right in this panel, sagittal, horizontal and axial plane view, focused on the parathymic region). The red full arrowhead shows the tracer accumulating part of the infiltrated lymph node, while the empty arrowhead points to the part of the enlarged lymph node not accumulating ^{67}Ga-citrate. (c) Ex-vivo Cerenkov image shows 67Ga-citrate accumulation in the previously identified part of the parathymic lymph node and low accumulation in the part identified with the empty arrowhead in SPECT/MRI. Scale bar corresponds to 1 cm. (d) Stereomicroscopic image of the same parathymic lymph node. Two areas are identified, * in the lower rectangle shows the tumor-infiltrated part, its histology analysis image indicated by a purple arrow, ** in the upper rectangle identifies the tumor infiltration border area in the lymph node. The corresponding immunohistochemistry image in (f) is pointed at with a red arrow. (e) Haematoxylin–eosin staining microscopy image of a section from the infiltrated part of the parathymic lymph node, identified with (a) * in (d). The sample is taken from the area in the lower rectangle of the stereomicroscopic image shown with *. Small clusters of residual normal lymphocytes (arrow) are visible, surrounded by large lymphoma infiltrates composed of irregularly shaped lymphoblasts (arrowhead). (f) Immunofluorescence histological image from the transitional area of the lymph node labeled **, delineated in the upper rectangle of the stereomicroscopic image in (e) demonstrates the remnant of original follicle composed of IgM/B220 double positive B cells adjacent to B220 single positive DLBCL cells (green: IgM, red: B220). Scale bar = 100 μm.

6.3 Preclinical studies 2: the investigation of tumor spreading in early and advanced stage

We have hypothesized that in the case of early tumor spreading (1 day post lymphoma inoculation) in the omentum and mesenterium, cell groups that do not have yet significant vascularization cannot be detected with an intravenously administered radiopharmaceutical. This raises the potential need for topical radiopharmaceutical administration in addition to intravenous diagnostic procedures and therapeutic approaches. Therefore, we tested our diagnostic approach using multiple modalities of imaging in the mouse Bc.DLFL1 lymphoma model. Our findings indicate that significant discrepancy exists between the detectability via intravenous or topical radiotracer application for the early monitoring of tumor progression.

6.3.1 Monitoring of early distribution of Bc.DLFL1 lymphoma cells after intraperitoneal inoculation using systemic and topical FDG administration

The typical radiotracer-based approach for in situ tumor detection employs the preferential uptake and cellular entrapment of FDG molecules by tumor cells. The high glucose utilization by most types of tumor cells is well-known. However we thought, -for effective early detection

of lymphoma cells- it is important to know the extent of FDG uptake in tumour cells compared with the FDG uptake in normal leukocytes. To assess the rate of FDG in Bc.DLFL1 cells, first we incubated freshly isolat-ed Bc.DLFL1 lymphoma cells in vitro in the presence of 100 kBq radioactivity of FDG, and compared their tracer uptake to that of normal mouse leukocytes in triplicate samples. The average FDG uptake was 48% of the original input activity by lymphoma cells, and 3% of the original activity by normal mouse mixed leukocytes, respectively. These observations indicate that Bc.DLFL1 lymphoma cells have a significantly higher capacity to take up FDG over normal mouse white blood cells, thus FDG appears a sensitive in vivo tracing tool for this lymphoma (Table 4).

4. Table 4. shows the results of mouse lymphoma cell and healthy mixed mouse leukocyte FDG uptake differences. Bc.DLFL1 lymphoma cells have a significantly higher capacity to take up FDG over normal mouse leukocytes

	BcDLFL.1 mouse lymphoma cells	**Healthy Mouse White Blood Cells**	**Mean Lymphoma to Healthy Cell Cell Uptake Proportions**
	Mean(SD) Ratio of Counts Per Minute	**Mean(SD) Ratio of Counts Per Minute**	14.77
Cell Pellet to Whole Incubate	47.56 (3.22)%	2.77 (2.22)%	

To determine whether in vivo PET imaging methods would allow monitoring of disease progression at the early stage, we used FDG for high grade lymphoma detection. We injected the Bc.DLFL1 lymphoma cells intraperitoneally, followed by the administration of the radiopharmaceutical 24 hours later either via intraperitoneal or intravenous injection. Using whole body PET scan we could not detect specific tracer accumulation in the early stage (1 day post-inoculation) after either intraperitoneal or intravenous tracer administration. To ensure that the tracer did reach the potential omental and mesenteric propagation sites, next we performed ex vivo autoradiography of the entire intestinal tract. We found that 2 hours after intraperitoneal FDG administration, several clearly marked foci were present within the mesentery or omentum in mice injected with Bc.DLFL1 cells; on the other hand, scanning after the intravenous injection of FDG no such pattern was detectable (Figure 11).

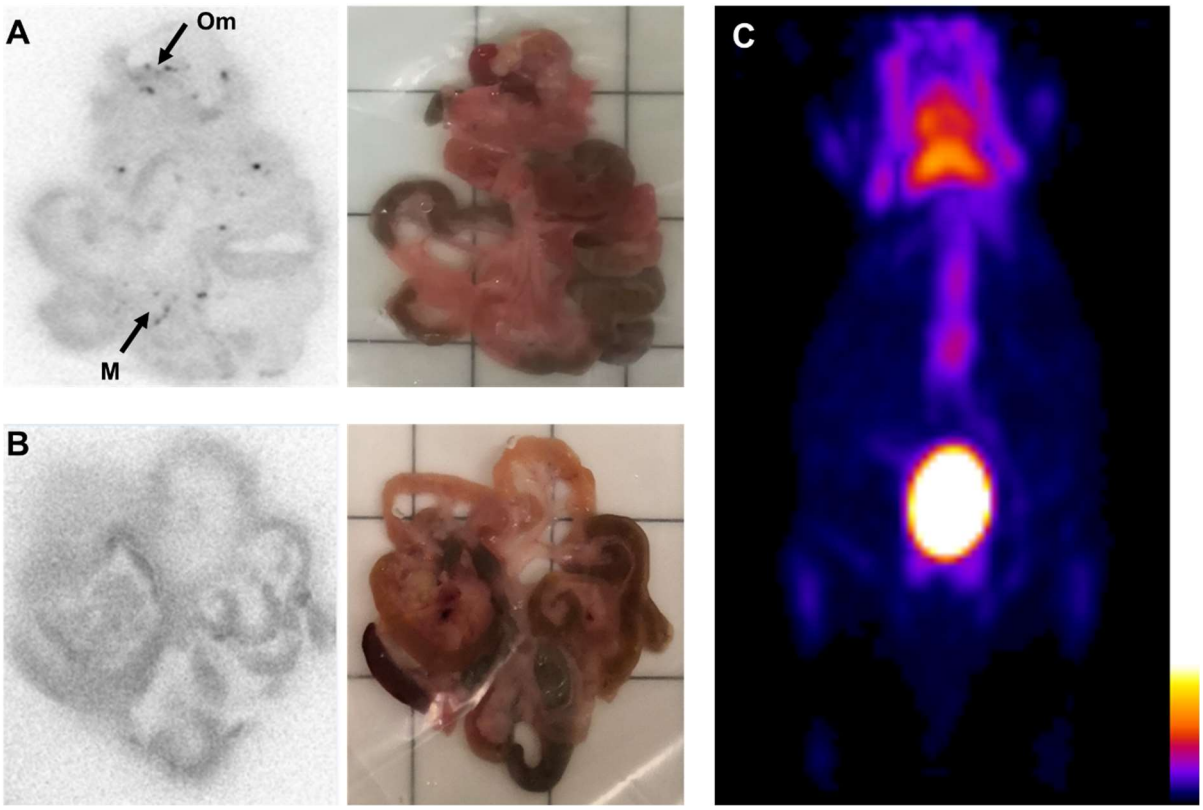

11 Figure 11: Intraperitoneal FDG is superior in detection to intravenously administered molecules in the early stage Bc.DLFL1 mouse lymphoma model. Ex vivo autoradiographic detection of the tumor cells 24 hours post intraperitoneal inoculation using i.p. FDG injection reveals cells adhered to the omentum (Om) and mesentery (M) placed to the ARG cassette (A). Intravenous administration of the radiotracer fails to identify mesentery- and omentum-associated lymphoma cells (B). The corresponding white light image panel is also presented for orientation (A-B). The lack of tumor-derived signal 24 hours after lymphoma inoculation is shown with a PET three-dimensional maximal intensity projection reconstruction acquired 2 hours following intraperitoneal FDG application. Only normal FDG mouse distribution is visible in the PET image (C).

To confirm that the selective focal omental and mesenteric ex vivo FDG signal is due to the previous local accumulation of lymphoma cells, we intraperitoneally injected BcDLFL.1 cells previously labelled with CFSE, and their distribution was monitored by immunohistochemical detection with an anti-FITC antibody. Using this technique, we found a labelling pattern matching the distribution observed by autoradiography in the omentum and the perivascular adipose cuffs surrounding the mesenteric arteries, as reported earlier [31, 32]. Thus, our in situ whole mount autoradiography results following intraperitoneal administration of FDG support the immunohistochemical data on the non-random early distribution of lymphoma cells (Figure 12 A, B, C). As a further confirmation of selective in vivo binding of CFSE-labelled lymphoma cells to the serosal lining, we used ex vivo confocal fiber optic fluorescent microscopy (Figure

12 D). We found that within the mesentery the CFSE-marked lymphoma cells show focal accumulation in a pattern like that observed with anti-FITC immunohistochemistry. Taken together, these findings indicate that although Bc.DLFL1 lymphoma cells clearly adhere to select peritoneal locations, their FDG tracing after either intravenous or intraperitoneal isotope administration does not permit in vivo lymphoma detection, while ex vivo FDG monitoring can reveal lymphoma accumulation after intraperitoneal tracer administration.

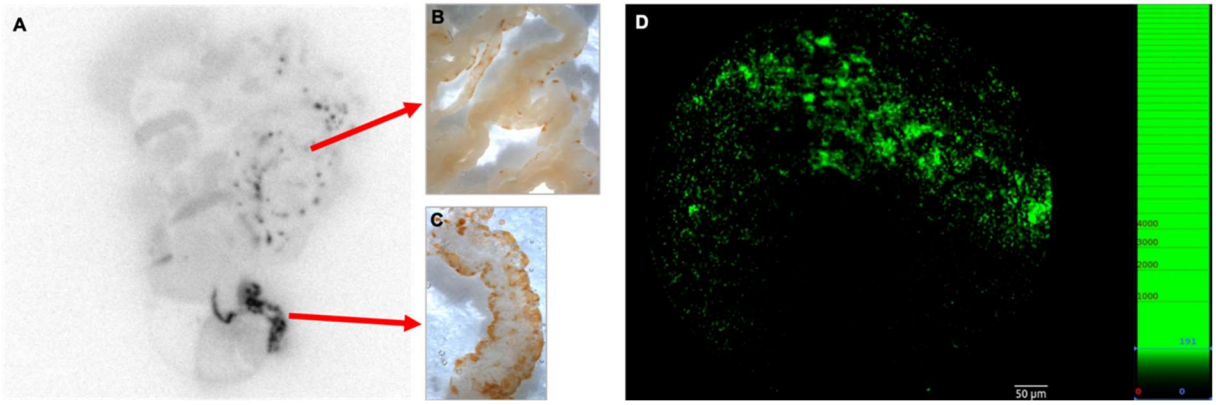

12. Figure 12: Multimodal correlated images of preferential sites during early lymphoma spreading. Correlation of ex vivo autoradiographic image of the abdominal organs (A) in a mouse 24 hours after intraperitoneal inoculation of 5x106 tumor cells (pre-loaded with CFSE dye) with the anti-FITC immunodetection (visualized as brown DAB precipitate) of lymphoma cells demonstrates a matching pattern in the mesentery and the omentum (B/C). The diagnostic radiotracer FDG molecule was injected ip two hours before imaging (n=9). Direct fluorescence visualization of fluorescein ex vivo using fluorescence confocal fiberoptic microscopy of the omentum reveals small to medium sized cell clusters (D).

6.3.2 Successful monitoring of lymphoma expansion in nodal metastasis by PET/MR and subsequent CLI in advanced stage

Our previous findings indicated the preferential expansion of Bc.DLFL1 lymphoma cells after intraperitoneal injection in the mesenteric lymph nodes (mLNs) and spleen. To monitor the expansion of tumor at late stage after the initial adhesion to serosal foci, we next tested whether PET or CLI would allow lymphoma detection after 7 day of inoculation. We found that, in contrast to the lack of radiopharmaceutical signal at the early lymphoma stage, a robust accumulation of FDG was detectable following the intravenous administration of tracer. The most intense labelling was observed using PET/MRI in the enlarged mLNs (Figure 13 A). On the other hand, this approach did not allow the separate visualization of the mesentery with the precise identification of mesenteric branches, which also harbor a substantial amount of lymphoma cells, as demonstrated by immunohistochemical analyses (Figure 14).

To improve the resolution of PET imaging of mesenteric branches, we employed Cerenkov Luminescence imaging as an ex vivo imaging modality with improved resolution. Using this approach we found luminescence signal linked to FGD accumulation in the omentum and in the adipose tissue along the mesenteric vessels and lymphatics, in addition to the intense signal from the enlarged mLNs (Figure 13 B). These findings reveal that at a later stage of lymphoma, the nodal metastases can be identified using PET/MRI even after the intravenous administration of tracer, but with only marginal separation of lymph nodes and surrounding adipose tissues of the mesenterium. On the other hand, application of CLI as an ex vivo test can sufficiently identify both nodal and adipose lymphoma infiltrates.

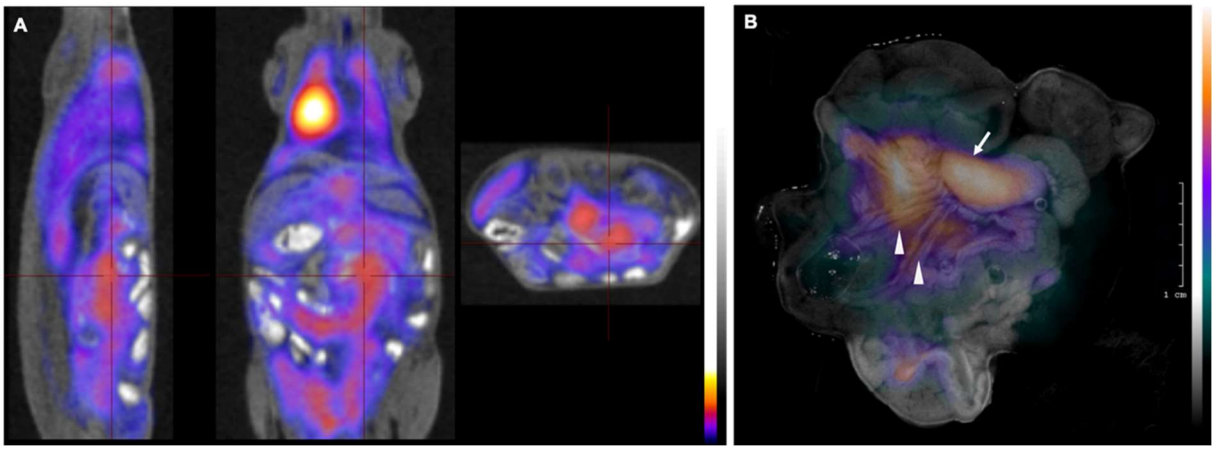

13. Figure 13: PET/MRI images of Bc-DLFL.1 lymphoma cell biodistribution in advanced stage. PET/MRI images of Bc.DLFL1 cell biodistribution at advanced lymphoma stage after ip tumor inoculation detected by intravenous FDG injection (administered 1 hour earlier) show several mesenteric lymph nodes accumulating (A). After subsequent removal, the abdominal organs were subjected to CLI ex vivo. Panel B shows superimposed white and Cerenkov light pictures. Arrow indicates extensive FDG accumulation in mesenteric lymph node conglomerates (arrow). In addition to mesenteric lymph nodes, CLI also detects the lymphoma expansion within mesenterial fatty streaks (arrowheads) (B).

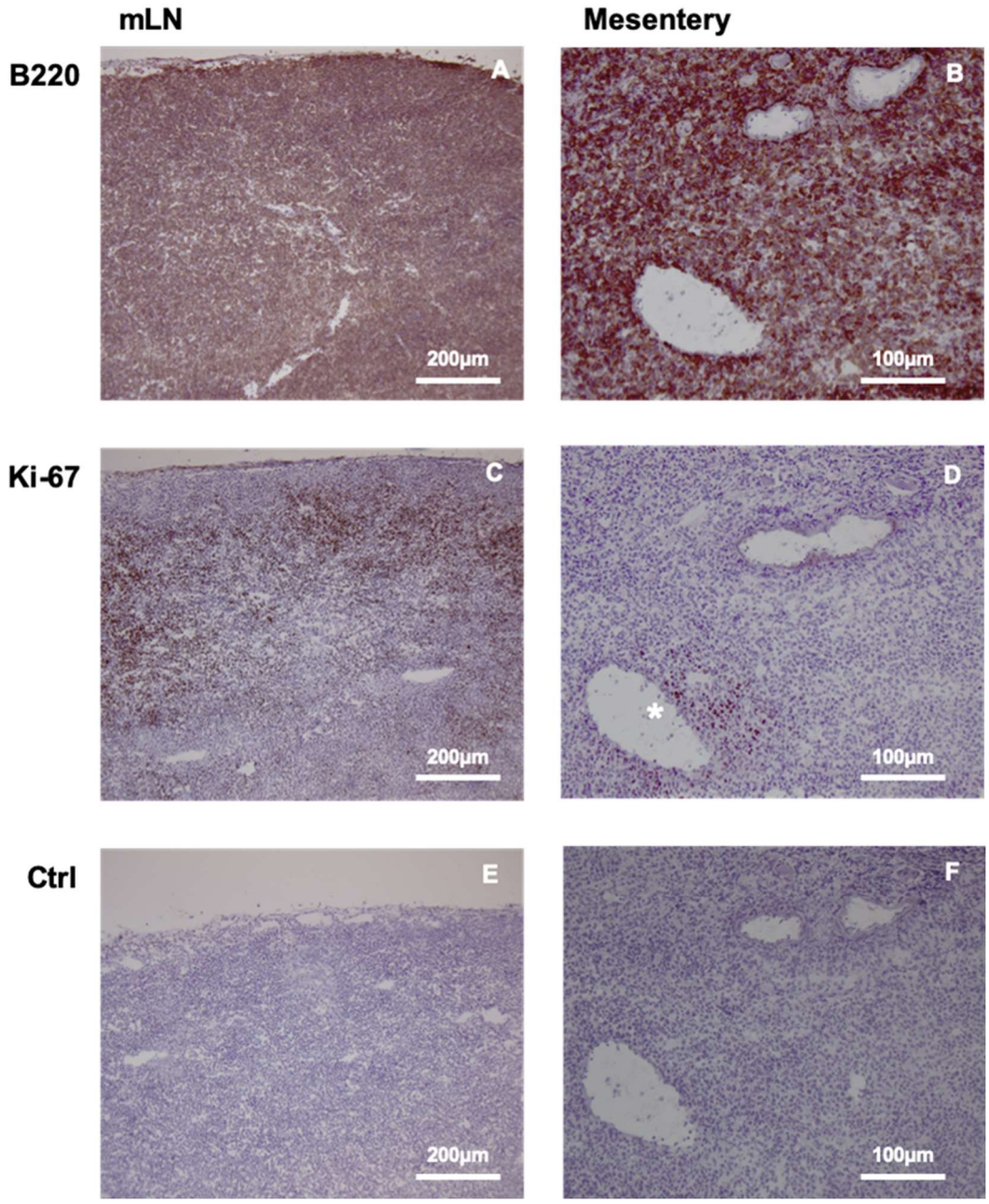

14. Figure 14: DLBCL accumulation and proliferation in mesenteric lymph node (mLN) and mesentery. B220 staining of mLN (A) demonstrates lymphoma expansion throughout the entire tissue, the expression of proliferation marker Ki-67 (C) reveals preferential proliferation in the cortical region, less prominent division is observed in the medullary area. Mesentery from also contains diffusely distributed B220-positive DLBCL cells (B), with dividing cells positive for Ki-67 marker restricted to the area surrounding the mesenteric vein (E) (labeled with *). Negative control staining of mLN and mesentery are shown in E/F.

7 Discussion

7.1 Clinical part

DLBCL is a heterogeneous disease at many levels with diverse genetic features and variable clinical outcomes [2, 10, 46]. Although the majority of DLBCL is potentially curable with standard treatment, there is an urgent need for new therapies since most refractory or relapsed patients will eventually die from the disease. Based on available data, about 40% of patients will be either resistant to initial line of therapy or will relapse after initial response. The majority of these patients cannot be salvaged by high-dose chemotherapy followed by ASCT and eventually will succumb to their disease. A better understanding of the pathogenesis of disease could help us understand the unique characteristics and the course of different subtypes of disease. Tremendous progress has been made over the past 20 years to identify the subtypes of DLBCL based on the cell of origin (COO), which carry significant impact on the prognosis of patients. In 2000, Alizadeh et al. [14] performed gene expression profiling with cDNA microarrays to explore the molecular heterogeneity in DLBCL. They described at least two distinct groups within DLBCL: the GCB group and the activated B-cell-like (ABC) or non-GCB group. This method has been widely recognized as the first COO based classification of DLBCL. In several randomized clinical trials following the establishment of COO classification by Alizadeh et al., DLBCL patients with the ABC subtype showed significantly poorer outcome compared with to those with the GCB subtype, even when the immune chemotherapy was used. In recent years, COO classification has been not only established as a prognostic factor but also used to target therapies for DLBCL patient. The World Health Organization (WHO) Classification for Lymphoid Malignancies requires the determination of COO for every newly diagnosed DLBCL case. In recent years, next-generation sequencing provides the possibility of more accurate classification of DLBCL. New DLBCL subgroups have been identified based on detailed molecular analysis, which may provide a more accurate prognosis prediction and pave the ways for personalized target therapy [5, 10, 16].

In connection with these recent advances in the molecular classification of lymphoma, several international trials have examined whether pretreatment baseline PET or interim PET imaging can separate poor-responder patients requiring intensification of therapy from good responders to the standard treatment [47-50].

The prognostic classification of DLBCL's patients was originally based on immunohistochemical and molecular genetic differences and laboratory and anamnestic data.

In addition to these parameters, the results of FDG-PET/CT have a strong and crucial prognostic significance. For the prognosis, the current evaluation of lymphoma and therapeutic efficacy in patients relies on Deauville scoring, using hepatic FDG uptake and mediastinal blood pool as reference value [19, 51, 52].

To optimize therapy for outcomes, many recently published papers propose that in addition to the Deauville scoring and delta SUV max, other semi-quantitative metabolic functional parameters from pretreatment functional imaging studies could be used including TMTV, and TLG, which have been mostly studied in DLBCL [53-55].

In addition to these parameters, it would be important to measure the tumor heterogeneity in lymphoma, which may also lead to a better prediction of prognosis. FDG-PET/CT is one of these non-invasive methods to examine the intratumor metabolic heterogeneity at a macroscopic scale [45, 56]. Many studies in different tumor types predicted additional prognostic outcome from textural parameters describing tumor heterogeneity [57]. Tumor heterogeneity in PET can be examined generally with the analysis of the histogram or the spatial arrangement of voxel intensities extracted by computational postprocessing techniques [26]. These parameters have been intensively studied in DLBCL and in other tumor types and seem to be also useful to select high-risk patient, but no definitive clinical metric proposal has been formed yet [58-63].

We aimed to investigate the potential prognostic significance of metabolic heterogeneity descriptors derived from primary PET and compare their diagnostic value with conventional PET metrics such as TMTV, TLG, and SUV max, and clinical data using multicenter automated machine learning analysis. We hypothesized that, we could identify and predict poor-responder patients, who may require additional molecular investigations, classification, and personalized, molecularly targeted treatment. For this, we retrospectively assessed the FDG-PET scans of 85 patients, which were performed in 2 clinical centers. The predictive model built on data from the first center resulted in 79% sensitivity, 83% specificity, 69% positive predictive value, 89% negative predictive value, 82% accuracy and an AUC of 0.85 on the second center dataset. Thus, based on clinical and imaging parameters determined before starting treatment, we were able to predict with high accuracy which patients would progress or relapse within 2 years of diagnosis. It is important to emphasize that the independent validation performance was higher utilizing Center 2 than the cross-validation performance within Center 1. This has multiple reasons: Center 1 was further split to subsets to conduct the cross-validation, which also

decreases predictability due to lower number of training subsets. Furthermore, the 100-fold Monte Carlo cross-validation scheme performs splitting randomly, which may result in training-validation subsets being less similar than the similarity of Center 1 and Center 2.

Our analysis determined prominent features to predict 2-year event-free survival. Based on the applied feature ranking, three volume-based biomarkers (TMTV, TLG and max diameter of the largest VOI) and two metabolic heterogeneity descriptors (NGTDM busyness and coarseness) had the highest diagnostic significance. Volume-based parameters refer to the extent of the lymphoma. The prognostic value of semi-quantitative metrics such as TMTV and TLG in lymphoma as well as in other tumor types has already been demonstrated [53-55]. In our study max diameter of the largest lymphoma foci appears to be a better prognosis predictor than the TMTV (see Supplemental: Feature importance). While these features may be redundant, their overall importance compared to each other may be different per cohort. Therefore, future investigations shall focus on identifying which of these two features are clinically relevant. While clinical parameters were included in our machine learning model-building process, feature ranking did not select them as relevant for predicting 2-years survival, compared to imaging features. As such, the highest-ranking clinical feature was R-IPI with the 12th rank and with a relative importance of 2.53%. This implies that 2-years survival can be predicted with imaging features, that may act as surrogates of, albeit being superior to clinical parameters.

According to the Imaging Biomarker Standardization Initiative (IBSI) „Textures with large changes in grey levels between neighboring voxels are said to be busy" [26]. If the busyness is high, the neighboring uptake change is sudden and not smooth. The violin plot shows that group 1 with poor prognosis has higher busyness values. This may be explained by the fact that lymphoma cells are embedded in a necrotic, sometimes hypoxic, periphery, which may be a key point of ineffectiveness of therapy, also because these regions may be more difficult to penetrate by the chemotherapeutic agent. Furthermore, Grey level differences in coarse textures are generally small due to large-scale patterns. Summing differences gives an indication of the level of the spatial rate of change in intensity. This means that high coarseness is associated with larger regions in the lesions, while low coarseness indicates that the texture subregions are smaller. The violin plot shows that group 1 with poor prognosis has lower coarseness values. Coarseness can be associated with cell diversities within the volume regarding their different FDG uptake, which can be due to less proliferative tumor cells or inhomogeneous tumor mass with necrosis and hypoxic area.

Aide et al. [58] predicted 2-year event-free survival in DLBCL, where the low grey high-level emphasis provided better prognosis prediction than TMTV, which may be due to population differences. However, Aide et al., did not evaluate features such as coarseness or busyness. In order to determine the real importance of these features, prospective studies with more DLBCL patients are needed.

In other – mostly solid – tumor types, coarseness was highlighted in predicting outcome of locally advanced rectum cancer [62]. In another study, both coarseness and busyness proved to be more predictive than other SUV based parameters in non-small cell lung cancer [64].

Among SUV-based metrics SUV-max is the most used parameter in routine diagnostics. With SUV max, indolent and aggressive lymphomas could be well-differentiated, and this metric is also correlated with tumor histology (proliferation rate) and blood levels of enzymes, for example KI-67 status and LDH [65]. Several research groups have already demonstrated the diagnostic value of SUV-max in lymphoma during primer staging, in one of them SUV-max proved to be more prognostic than TMTV or TLG [66]. However, in our study these parameters were less important features than others were. We hypothesized that the SUV measurements are more influenced by the instrumentations and environmental factors than volume-based and textural parameters.

In addition to PET parameters, clinical parameters are also crucial in the prediction of prognosis, and this fact was confirmed by our statistical approach even if these parameters had lower ranks than some PET parameters. Using Chi-square test results, we found a significant relationship between the DLBCL subtype groups and clinical and pathological parameters such as R-IPI and COO. Patients with non-GCB or higher R-IPI values have significantly worse 2 years prognosis as were reported in many previous studies. The prognostic value and diagnostic significance of COO and R-IPI have been known for very long time [4, 14]. The COO can be easily determined in all patients, mainly according to Hans algorithm, and its combination with TMTV has been suggested by some studies [67]. R-IPI proved to be more prognostic than TMTV in another study [68]. However, most of the studies use one or maximum two metrics for prognosis assessment [67, 69]. In contrast, machine learning-built prediction models have the potential to deliver more in-depth associations among clinical and PET data [70-72].

This study had limitations. First, we analyzed only the largest VOI in each patient with radiomics. Nevertheless, prior studies routinely analyzed the largest VOIs in DLBCL patients and yielded promising results [58, 61]. In addition, radiomic analysis is generally discouraged

to be performed involving small lesions. Second, our patient counts were relatively low in both Center 1 and Center 2 cohorts. Nevertheless, they were from different camera systems, that allowed to perform an independent validation scheme of our predictive model.

With our dual-center study, we could demonstrate that predicting two-years progression-free survival in DLBCL patients is feasible with high precision building on imaging and clinical parameters. This is in line with prior studies that utilize holistic datasets to build so-called holomics prediction models with machine learning [43, 73, 74]. Given that our model yielded a balanced sensitivity and specificity, it could be a viable option to personalize the patient's treatment. In the era of personalized medicine, with more detailed and specialized molecular diagnostics -especially in DLBCL- this could help the clinicians to manage their patients more adequately and effectively.

7.2 Preclinical studies 1: focus on CLI imaging

Over the past several decades, FDG-PET/CT has become the first line tool for the staging and monitoring of therapeutic efficiency in patients with high-grade malignant lymphomas. However, no definite diagnosis and well-directed therapy can be made in these patients, without a full biopsy of tumorous tissues, as cytology and fine needle aspirations are mostly inconclusive. A medical need for a sampling method also arose to identify a tumorous lymph node in a pre-planned manner with PET/CT images as basis. Tumour-infiltrated lymph node parts should be immediately localised and their targeted biopsy should be performed. In addition to the current sensitivity and resolution achievable by clinical FDG-PET are not adequate for monitoring fine details of tracer distribution within foci smaller than approximately 10 mm [75-77]. Other investigative methods such as autoradiography, fluorescence or bioluminescence imaging do not fit to any practical clinical context or they are simply not feasible in humans. Consequently, a sensitive, translatable sampling method applying the gold standard FDG tracer for DLBCL staging and therapeutic feedback remains a clinically important need. This development is effectively assisted validation of improved detection methodologies by translational pre-clinical mouse models. An ex vivo imaging measurement of metabolic heterogeneity in tumour tissue, in turn, could influence therapy planning, too. In our present work, we provide evidence for the potential radio-diagnostic application of the combination of PET imaging with *ex vivo* Cerenkov luminescence in an experimental high-grade B-cell lymphoma model. This combination provides a more detailed structural assessment of lymph nodes infiltrated by lymphoma cells at a more effective detection

sensitivity than any currently available in vivo tool, potentially also offering a much faster evaluation than via traditional processing by tissue histopathology [78, 79].

In addition, this model potentially allows the monitoring the effect of various experimental therapeutic approaches including measurements of metabolic heterogeneity of the tumour cell clusters within lymph nodes quickly after sampling. Combination of PET, SPECT, and CLI allows for this targeted sampling and detailed ex vivo testing. CLI can be used to examine several radioisotopes that are routinely used in the traditional clinical nuclear medicine toolkit [80-82].

The previously described, well-characterized high-grade mouse B-cell lymphoma model in our work has a restricted, stepwise in vivo propagation from the peritoneal cavity towards the environs of mesenteric lymph vessels into the mesenteric lymph nodes and then the spleen. [32]. This allowed us to image different locations of tumor spreading by using our proposed methodology.

We performed a multi-modal multi-tracer whole body in vivo imaging in a clinically relevant advanced stage of the animals with Bc.DLFL1 lymphoma load. This stage of the tumours was then imaged ex vivo using CLI, and the image details were compared to immunohistochemistry and microscopic results in the same animals. We decided to investigate ^{67}Ga-citrate, too, as i) this radiotracer is still the most specific and sensitive means for SPECT imaging of lymphoma [81], ii) modeling studies have shown an available Cerenkov luminescence from tissue ^{67}Ga distribution [35, 76] iii) there is a current re-emerging interest in ^{67}Ga as an Auger emitter`s therapeutic relevance [83].

To monitor the *in vivo* expansion of high-grade lymphoma, we tested whether the *in vivo* PET/MR and *ex vivo* CLI modality would allow lymphoma detection. We found that we could detect FDG accumulation in the organs infiltrated with lymphoma after intravenous administration of FDG and subsequent *in vivo* PET/MR and *ex vivo* CLI. This occurred at and after the advanced stage of lymphoma growth. Our ex vivo results suggest a new clinical application field of FDG detection using CLI for localisation and observation of the detailed metabolic heterogeneity of the affected lymph nodes. [81, 84-88].

To optimize therapy and plan for clinical monitoring, we propose that - besides Deauville scoring and the currently studied PET derived radiomics - it would be particularly important to obtain information about the heterogeneity of individual enlarged, tumorous lymph nodes. Measurement of glycolytic heterogeneities could lead to the identification of regions of tumor

stem cells within regions of lesser proliferative activity known to confer resistance to therapy. Of further importance are those heterogeneous tumor regions parts where the distribution of therapeutic drugs remains low, e.g. in peritoneal or retroperitoneal spread.

We report for the first time a successful high-contrast Cerenkov light imaging following the in vivo application of ^{67}Ga isotope. We assume that the origin of this Cerenkov luminescence is secondary electron spread generation in all tissue water compartments. Looking closer at the radionuclide`s high energy gamma emissions to initiate secondary electrons, we find gamma photons of 17% abundance at 300 keV and 5% abundance near 394 keV and other higher energies of 494, 703, 794, 814 below 0.1% and 888 keV at 0.1%, respectively, as reported in[89, 90]. An earlier calculated model of Cerenkov effects [35] has modeled an availability of 22%: 11 electrons per 50 disintegrations per ^{67}Ga-atom decay for the generation of secondary electrons in tissue or water, responsible for Cerenkov photon emission. A detectable number of photons per disintegration could be present, with slightly below 20% availability of Ga-67 Cerenkov Radiation efficiencies.

^{67}Ga-citrate scintigraphy played an important role in lymphoma monitoring earlier and still remains a very important diagnostic means in the majority of the world where PET/CTs are not available to this end. In Low-Income Countries, per million inhabitants, the number of SPECT scanners available is ten-fold compared to PET scanners. In Lower Middle Income, Middle Income and even High Income countries, this proportion is still in the significant range of two to four times the number of SPECT systems to PET [91]. Therefore, in countries and in regions without adequate access to PET scanners, ^{67}Ga-citrate could still remain an accessible specific radiopharmaceutical for lymphoma staging. The simplicity, low capital investment (circa a tenth to a fifth of any SPECT/CT system price) and low operational costs of CLI devices would provide clinical benefits to lower income countries.

We expected ^{67}Ga-citrate accumulation in Bc.DLFL1 lymphoma cells, supposing that ^{67}Ga-imaging of lymphoma can also provide information about the staging or monitoring the therapy response. In the clinics, many other studies have already demonstrated that FDG-PET is superior to ^{67}Ga-citrate imaging [92] in agreement with our study.

In summary, FDG-PET has proven to be more sensitive between the two radiopharmaceuticals in this model, as FDG-PET and Cerenkov imaging could visualize tumor foci in the abdomen in the advanced stage group of mice, while no such imaging possibility was feasible in the advanced stage group using ^{67}Ga-citrate, only in terminal stage animals. The reason for this can

be cell cycle heterogeneity of the tumour cell population. In earlier studies it has been shown that the tumoral cell over-expression of the molecule responsible for ^{67}Ga cellular uptake, i.e. the transferrin receptor (also referred to as CD71 glycoprotein) is cell-cycle dependent [93, 94]. On the other hand, overexpression and functions of glucose transport proteins are less dependent on the cell cycle phases. Theoretically, this offers a higher signal of increased glucose transporter detection in tumors than a ^{67}Ga uptake based detection relying on CD71 overexpression with fluctuating intensity. Another reason could be that the diagnostic performance of ^{67}Ga-citrate imaging is less accurate in case of small foci in the abdomen than in other part of the body due to the high intestinal background activity, but its use is justified in the supradiaphragmatic regions [29, 95, 96]. It has been shown in the present mouse lymphoma model study, too, that ^{67}Ga-citrate imaging would consequently be less sensitive than FDG-PET imaging. However, ^{67}Ga is an efficient therapeutic Auger electron emitter that has been applied in in vitro [97, 98], and also as a radionuclide with therapeutic potential in pre-clinical and preliminary clinical studies [83, 93, 94]. Using different targeted delivery methods to achieve specific cell nuclear uptake in lymphoma cells and DLBCL patients, ^{67}Ga might have a therapeutic potential in lymphoma, too. This could well be applied in conjunction with imaging of biodistribution spaces using CLI.

Our results confirmed the Cerenkov imaging suitability of ^{67}Ga-citrate. As ^{67}Ga decay emits both gamma radiation and can produce Cerenkov luminescence, it is applicable for both SPECT and CLI. Using this approach, we could locate a distant parathymic lymph node metastasis after intraperitoneal lymphoma injection with intravenous Ga-67 citrate administration followed by SPECT/MRI and *ex vivo* CLI. This metastatic location is in agreement with earlier demonstration of DLBCL lymphoma spreading following intraperitoneal injection [99]. However, further optimization strategies are needed to explore the full potential of this novel approach. During clinical translation, special care has to be taken for hospital staff radionuclide exposure. Observing as low as reasonably achievable (ALARA) radiation protection principles should be paramount regarding staff hazards when designing clinical experiments. Staff ALARA might be the most important challenge to large-scale CLI applications in the clinic.

7.3 Preclinical studies 2: the investigation of tumor spreading in early and advanced stage

The present work addresses the in vivo radio-imaging possibilities for the early detection of peritoneal spreading of a high-grade B-cell lymphoma in an experimental model. Although the specific molecular components, cell types, and mechanisms that lead to lymphatic spreading

and peritoneal metastasis of various tumors have been extensively studied [100-102], the specific conditions promoting the serosal propagation of lymphoid malignancies have not been completely understood, despite their reported appearance in abdominal adipose tissues [103]. Most frequently the tumors of the gastrointestinal tract and the ovaries may give rise to peritoneal metastases, but in the case of lymphomas, peritoneal or even mesenteric manifestations also commonly occur [103]. Therefore, our preclinical studies, performed in animal models in vivo and ex vivo, have the potential to translate diagnostic ideas and procedures to the clinical field to detect the spread of abdominal tumors. In addition, these findings may be extended to other malignancies with a more frequent occurrence of peritoneal metastases or extranodal manifestations in the abdominal cavity during the course of the disease. The detection of peritoneal metastases at an early stage could be a key component of effective therapy for these diseases [36, 37].

The restricted in vivo propagation of Bc-DLFL.1 lymphoma cells in the abdomen, and in mesenteric lymph nodes at advanced stage of the lymphoma was described previously [31]. Thus, we hypothesized that our well-characterized high-grade lymphoma isolated from BALB/c mice would be a suitable model for a preclinical investigation of various stages of abdominal tumor spread. To this end, we explored a combined molecular imaging approach, based on the widely available radiopharmaceutical FDG molecule.

The FDG molecule is the most frequently applied molecule used to diagnose high GLUT1-7 expression of human tumor cells related to their increased glycolysis. Compared to normal tissues, tumor cells have a greater utilization of glucose: These cells generally show increased expression of GLUT transporters (mainly GLUT-1 and GLUT-3 in lymphoma), higher hexokinase activity, and decreased or absent glucose 6 phosphatase activity [104-106]. Therefore, we first aimed to determine FDG uptake by murine lymphoma cells, comparing results with those of normal lymphocytes. The substantially higher, around 15-fold accumulation of FDG in vitro suggested its potential for tumor imaging difference in all stages, and made it unlikely that lymphocytes would be able to generate comparable signal strength. The main role of tumor cells in FDG uptake had been already pointed out in another study examining peritoneal tumor spread in mice [38].

We tried to investigate the early distribution pattern of high-grade B-cell lymphoma (Bc.DLFL1) using a functional imaging method that can also be applied in clinical diagnostics. It is important that in addition to staging of lymphoma and many other tumors, intravenous FDG has also been applied for the PET/CT diagnosis of peritoneal carcinosis, with various

reported specificities and sensitivities [107, 108]. In human diagnostics, FDG is always administered intravenously, and the imaging begins approximately 1–2 h after administration in subjects.

In our work, the failure to detect the serosal expansion of lymphoma by PET early after its inoculation can at least partly be attributed to the minuscule size of metastatic foci. These foci, with a size range of 0.1–0.2 mm, have a decreased contrast and are too small to work with, even using small animal PET instruments. In our early stage lymphoma monitoring, the size of tumor attached to the omental and mesenteric adipose tissue was clearly well below that of the lowest small animal PET resolution threshold of 0.7 mm [109]. In addition, while the serosal attachment sites for lymphoma binding contain a rich capillary meshwork [32], 24 h after intraperitoneal injection, only a few Bc.DLFL1 cells had entered the deeper vascularized parts of the adipose parenchyma. It seems plausible that initially, the low vascular supply due to the small size of serosal lymphocyte clusters combined with the low number of lymphoma cells that had entered the vascularized compartment, together hampered the initial identification of lymphoma adherence by intravenous FDG administration. Importantly, the vasculature in both omental and mesenteric milky spots displayed angiogenetic features [100]; thus, the subsequent invasion to these regions would probably allow for the intravenous tracing of lymphoma metastases at a later period. During the development of mouse molecular imaging techniques, the intraperitoneal administration of FDG has been proven to be a more convenient technique than intravenous injection, even though the clearance kinetics to the circulation are somewhat slower [110-112]. However, the detection of early intraperitoneal spread of tumors of such small sizes has not been performed in this way, even in mouse models [113-115]. The access of intravenously administered FDG to the early peritoneal metastatic foci is hampered by the lack of vasculature. At this early stage, the cells attached to the mesentery can proliferate, even in the absence of significant vascular supply, which can be explained by their reprogrammed metabolism [116] towards glycolysis. Although the initial adhesion territories were small, we found that the use of explant autoradiography with a better resolution potential [117, 118] could efficiently resolve the location of in vivo FDG-labeled foci matching whole-mount immunohistochemistry of CFSE-marked lymphoma cells and Cellvizio confocal fiber-optic imaging. Thus, the successful identification of initial metastatic locations required intraperitoneal delivery of FDG, and its detection with a more sensitive method such as autoradiography.

In the case of larger metastatic foci, which have a size detectable with clinical PET/CT (generally if the tumor diameter reaches approximately 5–6 mm [17, 18] the problem of low vascularization might still persist; however, even clinical PET would allow the detection of these foci if an appropriate (i.e., intraperitoneal) FDG transport route were to be used. Our work points out the possibility to expand the scope of PET/CT staging, by intraperitoneal tracer injection in tumors with peritoneal spread that might remain 'silent' if just intravenous FDG was applied. This may highlight the necessity for intraperitoneal delivery of tracer molecules in human subjects for more reliable identification of hitherto undetectable tumor colonies. This concept parallels the principles of local peritoneal administration of therapeutic compounds already in use [36, 119-121].

After a few days, intraperitoneally-injected lymphoma cells reach the mesenteric lymph nodes where they continue to proliferate. This is confirmed by intense Ki-67 expression, and also by the substantial enlargement of lymph nodes detectable after 7 days of lymphoma inoculation. At this stage, the metastatic mLNs have become resolvable, even after intravenous FDG administration with in vivo PET. It remains to be seen whether this increased FDG uptake at a later stage reflects lymphoma cell expansion only, or whether inflammatory infiltration by peritoneal macrophages also partly contributes to the enhanced signal, as previously described in a peritoneal adenocarcinoma model [38]. However, we observed contradictory findings between the lymphoma-filled mesentery by immunohistological results, and its less clearly defined imaging presentation by PET in live animals. As another opportunity for radioisotope detection of FDG, we chose to use CLI, which facilitated rapid evaluation [33, 85]. Positive PET scans also hinted at the presence of FDG-generated signals after the intravenous injection of tracer, due to the accumulation of lymphoma cells in vascularized mLNs, although their tissue resolution between mLNs and adjacent omental and mesenteric adipose tissues was unclear. The more precise resolution provided by the CLI approach could discriminate between the mLNs, serosal adipose tissue harboring lymphoma, and the burden-free intestinal tract. Similar to the radiodiagnostic approaches used at the early stage, at an advanced stage of lymphoma, the combined use of various imaging modalities may provide a more accurate readout of the tumor stage.

Even a decade ago, the first CLI imaging systems had a minimal detectable activity (MDA) figure of 45 kBq of FDG radioactivity in a volume of 0.3 mL for a 5 min scan time [85, 122]. The LightPath^{TM} system used in the study had an MDA of 20 kBq in a scan time of 100 s and a volume of 0.02 mL. The current clinical PET technology allows for the detection of 1 MBq

in 1 mL in a scan duration of 60 min (based on the authors' own clinical PET experience). This largely corresponds to at least one magnitude of gain in sensitivity when this CLI system is applied together with a PET scan. The image resolution gain is *par excellence* two orders of magnitude for CLI.

Translating our results to clinical practice might be directly feasible. The application of CLI in ex vivo samples could follow a PET scan within hours, or even in an overnight setting. The results of that preceding PET scan could direct the surgical removal of tumorous nodal samples. Thereafter, the exact nodal sample parts to be processed during pathology could be quickly read using the ex vivo CLI scans of those removed samples. The superior resolution and signal sensitivity of CLI might give an excellent indication of where exactly the metastatic foci may reside in a sample. However, practical clinical workflow limitations should be efficiently challenged during this translation. This could involve the just-in-time organization of PET scan, PET reading, and biopsies on the same day. Excessive physical sizes of other parenchymatous tumor samples would hamper Cerenkov light transmission; therefore, those should be addressed with special CLI and tissue preparational application protocols. The main physical limitation of the widespread use of CLI-PET combinations would, however, be healthcare staff radiation exposure.

8 The new results of the thesis

1. Analysis of a 2-years-event-free prediction model using radiomics derived from pre-treatment FDG-PET/CT in patients with DLBCL.

Based on our dual-center retrospective analysis, predicting 2-year EFS built on imaging features is feasible by utilizing high-performance automated machine learning. The most important image biomarkers for survival prediction were max diameter, TMTV, NGTDM coarseness, NGTDM busyness, and TLG. The SUV max, and clinical parameters were less prominent in our analysis. Therefore, subsequent DLBCL studies shall further evaluate the identified imaging biomarkers and their predictive performance in other clinical settings.

2. Development of a novel imaging tool combining PET/SPECT and CLI to be able to detect the most relevant affected lymph node and/or the most relevant part of the affected lymph node in a mouse model.

These results show that in vivo whole-body imaging with PET or SPECT, followed by ex vivo CLI acquisitions might be guiding tumor resection for pathology evaluation and therapy planning not only in preclinical investigations but for the clinical practice, too. CLI could be applied to outline tumorous tissues and to guide their surgical resection. Ex vivo CLI may guide the pathology sampling of any enlarged lymph nodes that have been previously localised by PET. Other surgically removed lymph nodes can be further investigated ex vivo. In this study context, we report Cerenkov imaging of ^{67}Ga isotope for the first time. The combined use of SPECT, PET and CLI in clinical oncological practice is warranted.

3. Select the most optimal nuclear medicine technique for early detection of peritoneal lymphoma spread using mouse model

Our clinically translatable findings point to the early detection possibilities and non-random metastatic route preferences of this lymphoma model. Local FDG administration should be given more consideration in radioisotopic diagnostic procedures. The adequate assessment of early peritoneal metastases in lymphoma, and perhaps clinically more importantly in colon, stomach or ovarian cancers, might be achieved this way. Topical diagnostic applications and the combination of imaging modalities are a clinically explorable method to promote more effective personalized topical therapy, in addition to systemic treatments. Cerenkov imaging translated to the clinic is one such avenue to achieve this.

9 Acknowledgments

First and foremost, I would like to mainly thank my supervisors Prof. Dr. Katalin Zámbó and Dr. Hussain Alizadeh for sharing their knowledge with me and supporting this interdisciplinary project throughout the entire process. I am also grateful for a lot of help and support from our head of division, Dr. Erzsébet Schmidt.

I truly appreciate that I had the opportunity to learn about small animal experiment and about imaging diagnostic in the preclinical field and study design from Dr. Domokos Máthé and Prof. Dr. Péter Balogh. I owe many thanks to Dr. László Papp who helped us with his advanced statistical knowledge and with designing and conducting the clinical part of our work.

I am grateful to Prof. Dr. Péter Németh for his great suggestions to my publications and research work. In additon to I owe many thanks for the other co-authors of my publications, and I would like to mention here Dr. Ferenc Budán, who helped me a lot with his suggestion to our work.

This work could not have been completed without the supportation of my wife and family.

10 Publications related to the dissertation

1. Zsombor Ritter, László Papp, Katalin Zámbó, Zoltán Tóth, Dániel Dezső, Dániel Sándor Veres, Domokos Máthé, Ferenc Budán, Éva Karádi, Anett Balikó, László Pajor, Árpád Szomor, Erzsébet Schmidt and Hussain Alizadeh, Two-Year Event-Free Survival Prediction in DLBCL Patients Based on In Vivo Radiomics and Clinical Parameters.

Frontiers in Oncology (2022) https://doi.org/10.3389/fonc.2022.820136 Q1, IF: 6,244

2. Zsombor Ritter, Katalin Zámbó, Péter Balogh, Dávid Szöllősi, Xinkai Jia, Ákos Balázs, Gabriella Taba, Dániel Dezső, Ildikó Horváth, Hussain Alizadeh, David Tuch, Kunal Vyas, Nikolett Hegedűs, Tibor Kovács, Krisztián Szigeti, Domokos Máthé & Erzsébet Schmidt, In situ lymphoma imaging in a spontaneous mouse model using the Cerenkov Luminescence of F-18 and Ga-67 isotopes.

Scientific Reports (2021) 11:24002 https://doi.org/10.1038/s41598-021-03505-3 D1, IF: 4,379

3. Zsombor Ritter, Katalin Zámbó, Xinkai Jia, Dávid Szöllosi, Dániel Dezso, Hussain Alizadeh, Ildikó Horváth, Nikolett Hegedus, David Tuch, Kunal Vyas, Péter Balogh, Domokos Máthé and Erzsébet Schmidt, Intraperitoneal Glucose Transport to Micrometastasis: A Multimodal In Vivo Imaging Investigation in a Mouse Lymphoma Model

International Journal of Molecular Sciences (2021) 22(9): 4431

https://doi.org/10.3390/ijms22094431 D1, IF: 5,924

Summarized IF: 16,546

10.1 Other Publications:

1. Zsolt Szakacs, Amar La Jorgen Kristensen, Nelli Farkas, Zsombor Ritter, Szabolcs Kiss, Anett Baliko, Hussain Alizadeh, 90Y-ibritumomab tiuxetan in B-cell non-Hodgkin lymphomas: Real-world data from the United Arab Emirates.

Advances in Radiation Oncology (2021) https://doi.org/10.1016/j.adro.2021.100882 Q2, IF: 2,655

2. Laszlo Szabo, Richard Molnar, Andras Tomesz, Arpad Deutsch, Richard Darago, Timea Varjas, Zsombor Ritter, Jozsef L. Szentpeteri, Kitti Andreidesz, Domokos Mathe, Imre Hegedüs, Attila Sik, Ferenc Budan, and Istvan Kiss, Olive Oil Improves While Trans Fatty Acids Further Aggravate the Hypomethylation of LINE-1 Retrotransposon DNA in an Environmental Carcinogen Model.

Nutrients (2022) 14:908. https://doi.org/10.3390/nu14040908 D1, IF: 5,719

Summarized IF: 8,374

10.2 Published Abstracts:

1 Z. Ritter, D. Máthé, P. Balogh, D. Szöllösi, I. Horváth, D. Tuch, K. Vyas, E. Schmidt, K. Zámbó, The investigation of the spreading of a novel spontaneous high grade lymphoma from BALB/c mice with CLI and different imaging modalities. EUROPEAN JOURNAL OF NUCLEAR MEDICINE AND MOLECULAR IMAGING (1619-7070 1619-7089): 45 Suppl. 1. pp S613-S613 (2018)

2 Ritter Z, Zambo K., Balogh P., Szollosi D., Xinkai J., Dezso D., Alizadeh H., Horvath I., Hegedus N., Mathe D., Schmidt E. The significance of intraperitoneal administration of 18F-FDG in a preclinical mouse model EUROPEAN JOURNAL OF NUCLEAR MEDICINE AND MOLECULAR IMAGING (1619-7070 1619-7089): 47 SUPPL 1 pp S644-S645 (2020)

3 Dezso D., Zambo K., Ritter Z., Ban Z., Szabo Z., Bodis B., Varady E., Szukits S., Toth A., Nemes O., Rucz K., Szujo S., Mezosi E., Bajnok L., Schmidt E., Measurement of epicardial adipose tissue with FDG-PET/CT in patients with type-2 diabetes mellitus EUROPEAN JOURNAL OF NUCLEAR MEDICINE AND MOLECULAR IMAGING (1619-7070 1619-7089): 46 SUPPL 1 pp S465-S465 (2019)

4 Ritter Z., Zambo K., Dezso D., Szabo Z., Ban Z., Kajtar B., Farkas K., Szomor A., Hussain A., Schmidt E., Clinical and prognostic significance of FDG-PET derived biomarkers in high grade B cell lymphoma. EUROPEAN JOURNAL OF NUCLEAR MEDICINE AND MOLECULAR IMAGING (1619-7070 1619-7089): 46 SUPPL 1 pp S565-S565 (2019)

5 Dezso D., Zambo K., Ritter Z., Ban Z., Szabo Z., Varady E., Bodis B., Nemes O., Rucz K., Szujo S., Mezosi E., Bajnok L., Schmidt E. Significance of epicardial and visceral adipose tissue measurement by 18F-FDG-PET / CT in type 2 diabetes mellitus. EUROPEAN

JOURNAL OF NUCLEAR MEDICINE AND MOLECULAR IMAGING (1619-7070 1619-7089): 47 SUPPL 1 pp S526-S527 (2020)

6 Ritter Z., Zambo K., Dezso D., Szabo Z., Ban Z., Szigeti K., Szollosi D., Veres D., Farkas K., Szomor A., Mathe D., Hussain A., Schmidt E., Prognostic significance of FDG-PET derived conventional and textural parameters in high grade B cell lymphoma EUROPEAN JOURNAL OF NUCLEAR MEDICINE AND MOLECULAR IMAGING (1619-7070 1619-7089): 48 SUPPL 1 pp S540-S541 (2021)

7 Dezso D., Zambo K., Ritter Z., Ban Z., Szabo Z., Schmidt E., Evaluation of incidental gastrointestinal accumulations in 18F-FDG PET to differentiate malignant lesions from benig ones. EUROPEAN JOURNAL OF NUCLEAR MEDICINE AND MOLECULAR IMAGING (1619-7070 1619-7089): 48 SUPPL 1 pp S528-S528 (2021)

11 References

1. Thandra KC, Barsouk A, Saginala K, Padala SA, Rawla P. Epidemiology of Non-Hodgkin's Lymphoma. Med Sci (Basel). 2021;9. doi:10.3390/medsci9010005.
2. Martelli M, Ferreri AJ, Agostinelli C, Di Rocco A, Pfreundschuh M, Pileri SA. Diffuse large B-cell lymphoma. Crit Rev Oncol Hematol. 2013;87:146-71. doi:10.1016/j.critrevonc.2012.12.009.
3. Swerdlow SH, Campo E, Pileri SA, Harris NL, Stein H, Siebert R, et al. The 2016 revision of the World Health Organization classification of lymphoid neoplasms. Blood. 2016;127:2375-90. doi:10.1182/blood-2016-01-643569.
4. Li S, Young KH, Medeiros LJ. Diffuse large B-cell lymphoma. Pathology. 2018;50:74-87. doi:10.1016/j.pathol.2017.09.006.
5. Abramson JS. Hitting back at lymphoma: How do modern diagnostics identify high-risk diffuse large B-cell lymphoma subsets and alter treatment? Cancer. 2019;125:3111-20. doi:10.1002/cncr.32145.
6. Sehn LH, Donaldson J, Chhanabhai M, Fitzgerald C, Gill K, Klasa R, et al. Introduction of combined CHOP plus rituximab therapy dramatically improved outcome of diffuse large B-cell lymphoma in British Columbia. J Clin Oncol. 2005;23:5027-33. doi:10.1200/JCO.2005.09.137.
7. Coiffier B, Thieblemont C, Van Den Neste E, Lepeu G, Plantier I, Castaigne S, et al. Long-term outcome of patients in the LNH-98.5 trial, the first randomized study comparing rituximab-CHOP to standard CHOP chemotherapy in DLBCL patients: a study by the Groupe d'Etudes des Lymphomes de l'Adulte. Blood. 2010;116:2040-5. doi:10.1182/blood-2010-03-276246.
8. Maurer MJ, Ghesquières H, Jais JP, Witzig TE, Haioun C, Thompson CA, et al. Event-free survival at 24 months is a robust end point for disease-related outcome in diffuse large B-cell lymphoma treated with immunochemotherapy. J Clin Oncol. 2014;32:1066-73. doi:10.1200/JCO.2013.51.5866.
9. Pasqualucci L, Dalla-Favera R. Genetics of diffuse large B-cell lymphoma. Blood. 2018;131:2307-19. doi:10.1182/blood-2017-11-764332.
10. Liu Y, Barta SK. Diffuse large B-cell lymphoma: 2019 update on diagnosis, risk stratification, and treatment. Am J Hematol. 2019;94:604-16. doi:10.1002/ajh.25460.
11. Kubuschok B, Held G, Pfreundschuh M. Management of diffuse large B-cell lymphoma (DLBCL). Cancer Treat Res. 2015;165:271-88. doi:10.1007/978-3-319-13150-4_11.
12. Caimi PF, Hill BT, Hsi ED, Smith MR. Clinical approach to diffuse large B cell lymphoma. Blood Rev. 2016;30:477-91. doi:10.1016/j.blre.2016.06.003.
13. Chaganti S, Illidge T, Barrington S, Mckay P, Linton K, Cwynarski K, et al. Guidelines for the management of diffuse large B-cell lymphoma. Br J Haematol. 2016;174:43-56. doi:10.1111/bjh.14136.
14. Alizadeh AA, Eisen MB, Davis RE, Ma C, Lossos IS, Rosenwald A, et al. Distinct types of diffuse large B-cell lymphoma identified by gene expression profiling. Nature. 2000;403:503-11. doi:10.1038/35000501.
15. Campo E, Swerdlow SH, Harris NL, Pileri S, Stein H, Jaffe ES. The 2008 WHO classification of lymphoid neoplasms and beyond: evolving concepts and practical applications. Blood. 2011;117:5019-32. doi:10.1182/blood-2011-01-293050.
16. Schmitz R, Wright GW, Huang DW, Johnson CA, Phelan JD, Wang JQ, et al. Genetics and Pathogenesis of Diffuse Large B-Cell Lymphoma. N Engl J Med. 2018;378:1396-407. doi:10.1056/NEJMoa1801445.
17. Boellaard R, O'Doherty MJ, Weber WA, Mottaghy FM, Lonsdale MN, Stroobants SG, et al. FDG PET and PET/CT: EANM procedure guidelines for tumour PET imaging: version 1.0. Eur J Nucl Med Mol Imaging. 2010;37:181-200. doi:10.1007/s00259-009-1297-4.
18. Boellaard R, Delgado-Bolton R, Oyen WJ, Giammarile F, Tatsch K, Eschner W, et al. FDG PET/CT: EANM procedure guidelines for tumour imaging: version 2.0. Eur J Nucl Med Mol Imaging. 2015;42:328-54. doi:10.1007/s00259-014-2961-x.
19. Cheson BD, Fisher RI, Barrington SF, Cavalli F, Schwartz LH, Zucca E, et al. Recommendations for initial evaluation, staging, and response assessment of Hodgkin and non-Hodgkin lymphoma: the Lugano classification. J Clin Oncol. 2014;32:3059-68. doi:10.1200/JCO.2013.54.8800.
20. Cerci JJ, Tabacchi E, Bogoni M. Fluorodeoxyglucose-PET/Computed Tomography-Guided Biopsy. PET Clin. 2016;11:57-64. doi:10.1016/j.cpet.2015.08.001.

21. El-Galaly TC, Villa D, Gormsen LC, Baech J, Lo A, Cheah CY. FDG-PET/CT in the management of lymphomas: current status and future directions. J Intern Med. 2018;284:358-76. doi:10.1111/joim.12813.
22. Voltin CA, Mettler J, Grosse J, Dietlein M, Baues C, Schmitz C, et al. FDG-PET Imaging for Hodgkin and Diffuse Large B-Cell Lymphoma-An Updated Overview. Cancers (Basel). 2020;12. doi:10.3390/cancers12030601.
23. Gisselbrecht C, Van Den Neste E. How I manage patients with relapsed/refractory diffuse large B cell lymphoma. Br J Haematol. 2018;182:633-43. doi:10.1111/bjh.15412.
24. Thieblemont C, Bernard S, Meignan M, Molina T. Optimizing initial therapy in DLBCL. Best Pract Res Clin Haematol. 2018;31:199-208. doi:10.1016/j.beha.2018.08.001.
25. Papp L, Spielvogel CP, Rausch I, Hacker M, Beyer T. Personalizing Medicine Through Hybrid Imaging and Medical Big Data Analysis. Frontiers in Physics. 2018;6:19. doi:10.3389/fphy.2018.00051.
26. Mayerhoefer ME, Materka A, Langs G, Häggström I, Szczypiński P, Gibbs P, et al. Introduction to Radiomics. J Nucl Med. 2020;61:488-95. doi:10.2967/jnumed.118.222893.
27. Traverso A, Wee L, Dekker A, Gillies R. Repeatability and Reproducibility of Radiomic Features: A Systematic Review. Int J Radiat Oncol Biol Phys. 2018;102:1143-58. doi:10.1016/j.ijrobp.2018.05.053.
28. Zwanenburg A, Vallières M, Abdalah MA, Aerts HJWL, Andrearczyk V, Apte A, et al. The Image Biomarker Standardization Initiative: Standardized Quantitative Radiomics for High-Throughput Image-based Phenotyping. Radiology. 2020;295:328-38. doi:10.1148/radiol.2020191145.
29. England CG, Rui L, Cai W. Lymphoma: current status of clinical and preclinical imaging with radiolabeled antibodies. Eur J Nucl Med Mol Imaging. 2017;44:517-32. doi:10.1007/s00259-016-3560-9.
30. Mc Larney B, Skubal M, Grimm J. A Review of Recent and Emerging Approaches for the Clinical Application of Cerenkov Luminescence Imaging. Frontiers in Physics. 2021;9. doi:10.3389/fphy.2021.684196.
31. Vojkovics D, Kellermayer Z, Heidt D, Mihalj M, Kajtár B, Ernszt D, et al. Isolation and Characterization of a Murine Spontaneous High-Grade Follicular Lymphoma with Restricted In Vivo Spreading--a Model for Lymphatic Metastasis Via the Mesentery. Pathol Oncol Res. 2016;22:421-30. doi:10.1007/s12253-015-0025-6.
32. Jia X, Gábris F, Jacobsen Ó, Bedics G, Botz B, Helyes Z, et al. Foliate Lymphoid Aggregates as Novel Forms of Serous Lymphocyte Entry Sites of Peritoneal B Cells and High-Grade B Cell Lymphomas. J Immunol. 2020;204:23-36. doi:10.4049/jimmunol.1900851.
33. Mitchell GS, Gill RK, Boucher DL, Li C, Cherry SR. In vivo Cerenkov luminescence imaging: a new tool for molecular imaging. Philos Trans A Math Phys Eng Sci. 2011;369:4605-19. doi:10.1098/rsta.2011.0271.
34. Chin PT, Welling MM, Meskers SC, Valdes Olmos RA, Tanke H, van Leeuwen FW. Optical imaging as an expansion of nuclear medicine: Cerenkov-based luminescence vs fluorescence-based luminescence. Eur J Nucl Med Mol Imaging. 2013;40:1283-91. doi:10.1007/s00259-013-2408-9.
35. Beattie BJ, Thorek DL, Schmidtlein CR, Pentlow KS, Humm JL, Hielscher AH. Quantitative modeling of Cerenkov light production efficiency from medical radionuclides. PLoS One. 2012;7:e31402. doi:10.1371/journal.pone.0031402.
36. Lungoci C, Mironiuc AI, Muntean V, Oniu T, Leebmann H, Mayr M, et al. Multimodality treatment strategies have changed prognosis of peritoneal metastases. World J Gastrointest Oncol. 2016;8:67-82. doi:10.4251/wjgo.v8.i1.67.
37. Narasimhan V, Ooi G, Michael M, Ramsay R, Lynch C, Heriot A. Colorectal peritoneal metastases: pathogenesis, diagnosis and treatment options - an evidence-based update. ANZ J Surg. 2020;90:1592-7. doi:10.1111/ans.15796.
38. Cottone L, Valtorta S, Capobianco A, Belloli S, Rovere-Querini P, Fazio F, et al. Evaluation of the role of tumor-associated macrophages in an experimental model of peritoneal carcinomatosis using (18)F-FDG PET. J Nucl Med. 2011;52:1770-7. doi:10.2967/jnumed.111.089177.
39. Hans CP, Weisenburger DD, Greiner TC, Gascoyne RD, Delabie J, Ott G, et al. Confirmation of the molecular classification of diffuse large B-cell lymphoma by immunohistochemistry using a tissue microarray. Blood. 2004;103:275-82. doi:10.1182/blood-2003-05-1545.

40. Cheson BD, Pfistner B, Juweid ME, Gascoyne RD, Specht L, Horning SJ, et al. Revised response criteria for malignant lymphoma. J Clin Oncol. 2007;25:579-86. doi:10.1200/JCO.2006.09.2403.
41. Eude F, Toledano MN, Vera P, Tilly H, Mihailescu SD, Becker S. Reproducibility of Baseline Tumour Metabolic Volume Measurements in Diffuse Large B-Cell LymphomA: Is There a Superior Method? Metabolites. 2021;11. doi:10.3390/metabo11020072.
42. Kinahan PE, Fletcher JW. Positron emission tomography-computed tomography standardized uptake values in clinical practice and assessing response to therapy. Semin Ultrasound CT MR. 2010;31:496-505. doi:10.1053/j.sult.2010.10.001.
43. Papp L, Spielvogel CP, Grubmüller B, Grahovac M, Krajnc D, Ecsedi B, et al. Supervised machine learning enables non-invasive lesion characterization in primary prostate cancer with [68Ga]Ga-PSMA-11 PET/MRI [Eur J Nucl Med Mol Imaging. 2021;48:1795-805. doi:10.1007/s00259-020-05140-y.
44. Papp L, Pötsch N, Grahovac M, Schmidbauer V, Woehrer A, Preusser M, et al. Glioma Survival Prediction with Combined Analysis of In Vivo 11 C-MET PET Features, Ex Vivo Features, and Patient Features by Supervised Machine Learning. J Nucl Med. 2018;59:892-9. doi:10.2967/jnumed.117.202267.
45. Ibrahim A, Vallières M, Woodruff H, Primakov S, Beheshti M, Keek S, et al. Radiomics Analysis for Clinical Decision Support in Nuclear Medicine. Semin Nucl Med. 2019;49:438-49. doi:10.1053/j.semnuclmed.2019.06.005.
46. Perry AM, Diebold J, Nathwani BN, MacLennan KA, Müller-Hermelink HK, Bast M, et al. Non-Hodgkin lymphoma in the developing world: review of 4539 cases from the International Non-Hodgkin Lymphoma Classification Project. Haematologica. 2016;101:1244-50. doi:10.3324/haematol.2016.148809.
47. Freeman CL, Savage KJ, Villa DR, Scott DW, Srour L, Gerrie AS, et al. Long-term results of PET-guided radiation in patients with advanced-stage diffuse large B-cell lymphoma treated with R-CHOP. Blood. 2021;137:929-38. doi:10.1182/blood.2020005846.
48. Dührsen U, Müller S, Hertenstein B, Thomssen H, Kotzerke J, Mesters R, et al. Positron Emission Tomography-Guided Therapy of Aggressive Non-Hodgkin Lymphomas (PETAL): A Multicenter, Randomized Phase III Trial. J Clin Oncol. 2018;36:2024-34. doi:10.1200/JCO.2017.76.8093.
49. Hüttmann A, Rekowski J, Müller SP, Hertenstein B, Franzius C, Mesters R, et al. Six versus eight doses of rituximab in patients with aggressive B cell lymphoma receiving six cycles of CHOP: results from the "Positron Emission Tomography-Guided Therapy of Aggressive Non-Hodgkin Lymphomas" (PETAL) trial. Ann Hematol. 2019;98:897-907. doi:10.1007/s00277-018-3578-0.
50. Zucca E, Cascione L, Ruberto T, Facchinelli D, Schär S, Hayoz S, et al. Prognostic models integrating quantitative parameters from baseline and interim positron emission computed tomography in patients with diffuse large B-cell lymphoma: post-hoc analysis from the SAKK38/07 clinical trial. Hematol Oncol. 2020;38:715-25. doi:10.1002/hon.2805.
51. Cheson BD. Staging and response assessment in lymphomas: the new Lugano classification. Chin Clin Oncol. 2015;4:5. doi:10.3978/j.issn.2304-3865.2014.11.03.
52. Barrington SF, Mikhaeel NG, Kostakoglu L, Meignan M, Hutchings M, Müeller SP, et al. Role of imaging in the staging and response assessment of lymphoma: consensus of the International Conference on Malignant Lymphomas Imaging Working Group. J Clin Oncol. 2014;32:3048-58. doi:10.1200/JCO.2013.53.5229.
53. Vercellino L, Cottereau AS, Casasnovas O, Tilly H, Feugier P, Chartier L, et al. High total metabolic tumor volume at baseline predicts survival independent of response to therapy. Blood. 2020;135:1396-405. doi:10.1182/blood.2019003526.
54. Kostakoglu L, Chauvie S. PET-Derived Quantitative Metrics for Response and Prognosis in Lymphoma. PET Clin. 2019;14:317-29. doi:10.1016/j.cpet.2019.03.002.
55. Prieto Prieto JC, Vallejo Casas JA, Hatzimichael E, Fotopoulos A, Kiortsis DN, Sioka C. The contribution of metabolic parameters of FDG PET/CT prior and during therapy of adult patients with lymphomas. Ann Nucl Med. 2020;34:707-17. doi:10.1007/s12149-020-01521-3.

56. Bailly C, Bodet-Milin C, Bourgeois M, Gouard S, Ansquer C, Barbaud M, et al. Exploring Tumor Heterogeneity Using PET Imaging: The Big Picture. Cancers (Basel). 2019;11. doi:10.3390/cancers11091282.
57. Mayerhoefer ME, Umutlu L, Schöder H. Functional imaging using radiomic features in assessment of lymphoma. Methods. 2021;188:105-11. doi:10.1016/j.ymeth.2020.06.020.
58. Aide N, Fruchart C, Nganoa C, Gac AC, Lasnon C. Baseline 18 F-FDG PET radiomic features as predictors of 2-year event-free survival in diffuse large B cell lymphomas treated with immunochemotherapy. Eur Radiol. 2020;30:4623-32. doi:10.1007/s00330-020-06815-8.
59. Zhou Y, Ma XL, Pu LT, Zhou RF, Ou XJ, Tian R. Prediction of Overall Survival and Progression-Free Survival by the. Contrast Media Mol Imaging. 2019;2019:5963607. doi:10.1155/2019/5963607.
60. Sun Y, Qiao X, Jiang C, Liu S, Zhou Z. Texture Analysis Improves the Value of Pretreatment. Contrast Media Mol Imaging. 2020;2020:2981585. doi:10.1155/2020/2981585.
61. Senjo H, Hirata K, Izumiyama K, Minauchi K, Tsukamoto E, Itoh K, et al. High metabolic heterogeneity on baseline 18FDG-PET/CT scan as a poor prognostic factor for newly diagnosed diffuse large B-cell lymphoma. Blood Adv. 2020;4:2286-96. doi:10.1182/bloodadvances.2020001816.
62. Lovinfosse P, Polus M, Van Daele D, Martinive P, Daenen F, Hatt M, et al. FDG PET/CT radiomics for predicting the outcome of locally advanced rectal cancer. Eur J Nucl Med Mol Imaging. 2018;45:365-75. doi:10.1007/s00259-017-3855-5.
63. Park S, Ha S, Lee SH, Paeng JC, Keam B, Kim TM, et al. Intratumoral heterogeneity characterized by pretreatment PET in non-small cell lung cancer patients predicts progression-free survival on EGFR tyrosine kinase inhibitor. PLoS One. 2018;13:e0189766. doi:10.1371/journal.pone.0189766.
64. Cook GJ, Yip C, Siddique M, Goh V, Chicklore S, Roy A, et al. Are pretreatment 18F-FDG PET tumor textural features in non-small cell lung cancer associated with response and survival after chemoradiotherapy? J Nucl Med. 2013;54:19-26. doi:10.2967/jnumed.112.107375.
65. Kostakoglu L, Chauvie S. Metabolic Tumor Volume Metrics in Lymphoma. Semin Nucl Med. 2018;48:50-66. doi:10.1053/j.semnuclmed.2017.09.005.
66. Gallicchio R, Mansueto G, Simeon V, Nardelli A, Guariglia R, Capacchione D, et al. F-18 FDG PET/CT quantization parameters as predictors of outcome in patients with diffuse large B-cell lymphoma. Eur J Haematol. 2014;92:382-9. doi:10.1111/ejh.12268.
67. Cottereau AS, Lanic H, Mareschal S, Meignan M, Vera P, Tilly H, et al. Molecular Profile and FDG-PET/CT Total Metabolic Tumor Volume Improve Risk Classification at Diagnosis for Patients with Diffuse Large B-Cell Lymphoma. Clin Cancer Res. 2016;22:3801-9. doi:10.1158/1078-0432.CCR-15-2825.
68. Adams HJ, de Klerk JM, Fijnheer R, Heggelman BG, Dubois SV, Nievelstein RA, et al. Prognostic superiority of the National Comprehensive Cancer Network International Prognostic Index over pretreatment whole-body volumetric-metabolic FDG-PET/CT metrics in diffuse large B-cell lymphoma. Eur J Haematol. 2015;94:532-9. doi:10.1111/ejh.12467.
69. Cottereau AS, Nioche C, Dirand AS, Clerc J, Morschhauser F, Casasnovas O, et al. F-FDG PET Dissemination Features in Diffuse Large B-Cell Lymphoma Are Predictive of Outcome. J Nucl Med. 2020;61:40-5. doi:10.2967/jnumed.119.229450.
70. Toyama Y, Hotta M, Motoi F, Takanami K, Minamimoto R, Takase K. Prognostic value of FDG-PET radiomics with machine learning in pancreatic cancer. Sci Rep. 2020;10:17024. doi:10.1038/s41598-020-73237-3.
71. Ahn HK, Lee H, Kim SG, Hyun SH. Pre-treatment. Clin Radiol. 2019;74:467-73. doi:10.1016/j.crad.2019.02.008.
72. Zhong J, Frood R, Brown P, Nelstrop H, Prestwich R, McDermott G, et al. Machine learning-based FDG PET-CT radiomics for outcome prediction in larynx and hypopharynx squamous cell carcinoma. Clin Radiol. 2021;76:78.e9-.e17. doi:10.1016/j.crad.2020.08.030.
73. Laszlo Papp CPS, Ivo Rausch, Marcus Hacker, Thomas Beyer. Personalizing Medicine Through Hybrid Imaging and Medical Big Data Analysis. Frontiers in Physics. 2018;60. doi:10.3389/fphy.2018.00051.
74. Krajnc D, Papp L, Nakuz TS, Magometschnigg HF, Grahovac M, Spielvogel CP, et al. Breast Tumor Characterization Using [Cancers (Basel). 2021;13. doi:10.3390/cancers13061249.

75. Cheebsumon P, Yaqub M, van Velden FH, Hoekstra OS, Lammertsma AA, Boellaard R. Impact of [^{18}F]FDG PET imaging parameters on automatic tumour delineation: need for improved tumour delineation methodology. Eur J Nucl Med Mol Imaging. 2011;38:2136-44. doi:10.1007/s00259-011-1899-5.
76. Chicklore S, Goh V, Siddique M, Roy A, Marsden PK, Cook GJ. Quantifying tumour heterogeneity in 18F-FDG PET/CT imaging by texture analysis. Eur J Nucl Med Mol Imaging. 2013;40:133-40. doi:10.1007/s00259-012-2247-0.
77. Spinelli AE, Boschi F. Novel biomedical applications of Cerenkov radiation and radioluminescence imaging. Phys Med. 2015;31:120-9. doi:10.1016/j.ejmp.2014.12.003.
78. Olde Heuvel J, de Wit-van der Veen BJ, van der Poel HG, Bekers EM, Grootendorst MR, Vyas KN, et al. Ga-PSMA Cerenkov luminescence imaging in primary prostate cancer: first-in-man series. Eur J Nucl Med Mol Imaging. 2020;47:2624-32. doi:10.1007/s00259-020-04783-1.
79. Grootendorst MR, Cariati M, Pinder SE, Kothari A, Douek M, Kovacs T, et al. Intraoperative Assessment of Tumor Resection Margins in Breast-Conserving Surgery Using. J Nucl Med. 2017;58:891-8. doi:10.2967/jnumed.116.181032.
80. D'Souza JW, Hensley H, Doss M, Beigarten C, Torgov M, Olafsen T, et al. Cerenkov Luminescence Imaging as a Modality to Evaluate Antibody-Based PET Radiotracers. J Nucl Med. 2017;58:175-80. doi:10.2967/jnumed.116.178780.
81. Dorth JA, Chino JP, Prosnitz LR, Diehl LF, Beaven AW, Coleman RE, et al. The impact of radiation therapy in patients with diffuse large B-cell lymphoma with positive post-chemotherapy FDG-PET or gallium-67 scans. Ann Oncol. 2011;22:405-10. doi:10.1093/annonc/mdq389.
82. Holland JP, Normand G, Ruggiero A, Lewis JS, Grimm J. Intraoperative imaging of positron emission tomographic radiotracers using Cerenkov luminescence emissions. Mol Imaging. 2011;10:177-86, 1-3.
83. Ku A, Facca VJ, Cai Z, Reilly RM. Auger electrons for cancer therapy - a review. EJNMMI Radiopharm Chem. 2019;4:27. doi:10.1186/s41181-019-0075-2.
84. Grootendorst MR, Cariati M, Kothari A, Tuch DS, Purushotham A. Cerenkov luminescence imaging (CLI) for image-guided cancer surgery. Clin Transl Imaging. 2016;4:353-66. doi:10.1007/s40336-016-0183-x.
85. Tamura R, Pratt EC, Grimm J. Innovations in Nuclear Imaging Instrumentation: Cerenkov Imaging. Semin Nucl Med. 2018;48:359-66. doi:10.1053/j.semnuclmed.2018.02.007.
86. Zhang Z, Cai M, Bao C, Hu Z, Tian J. Endoscopic Cerenkov luminescence imaging and image-guided tumor resection on hepatocellular carcinoma-bearing mouse models. Nanomedicine. 2019;17:62-70. doi:10.1016/j.nano.2018.12.017.
87. Lewis DY, Mair R, Wright A, Allinson K, Lyons SK, Booth T, et al. [Theranostics. 2018;8:3991-4002. doi:10.7150/thno.23709.
88. Boschi F, De Sanctis F, Ugel S, Spinelli AE. T-cell tracking using Cerenkov and radioluminescence imaging. J Biophotonics. 2018;11:e201800093. doi:10.1002/jbio.201800093.
89. Govindan SV, Goldenberg DM, Elsamra SE, Griffiths GL, Ong GL, Brechbiel MW, et al. Radionuclides linked to a CD74 antibody as therapeutic agents for B-cell lymphoma: comparison of Auger electron emitters with beta-particle emitters. J Nucl Med. 2000;41:2089-97.
90. Koumarianou E, Slastnikova TA, Pruszynski M, Rosenkranz AA, Vaidyanathan G, Sobolev AS, et al. Radiolabeling and in vitro evaluation of (67)Ga-NOTA-modular nanotransporter--a potential Auger electron emitting EGFR-targeted radiotherapeutic. Nucl Med Biol. 2014;41:441-9. doi:10.1016/j.nucmedbio.2014.03.026.
91. Paez D, Giammarile F, Orellana P. Nuclear medicine: a global perspective. Clinical and Translational Imaging. 2020;8:51-3. doi:10.1007/s40336-020-00359-z.
92. Cheson BD. PET/CT in Lymphoma: Current Overview and Future Directions. Semin Nucl Med. 2018;48:76-81. doi:10.1053/j.semnuclmed.2017.09.007.
93. Jonkhoff AR, Plaizier MA, Ossenkoppele GJ, Teule GJ, Huijgens PC. High-dose gallium-67 therapy in patients with relapsed acute leukaemia: a feasibility study. Br J Cancer. 1995;72:1541-6. doi:10.1038/bjc.1995.544.
94. Huijgens PC, Jonkhoff AR, Hoekstra OS, Ossenkoppele GJ, Teule GJ. Therapeutic potential of intravenous 67-gallium in non-Hodgkin's lymphoma. Eur J Haematol. 1993;51:206-8. doi:10.1111/j.1600-0609.1993.tb00631.x.

95. Even-Sapir E, Israel O. Gallium-67 scintigraphy: a cornerstone in functional imaging of lymphoma. Eur J Nucl Med Mol Imaging. 2003;30 Suppl 1:S65-81. doi:10.1007/s00259-003-1164-7.
96. Sakurai M, Toyama T, Kikuchi T, Kato J, Shimizu T, Koda Y, et al. Comparison of fluorine-18 fluorodeoxyglucose positron emission tomography with gallium-67 scintigraphy in the initial clinical staging of diffuse large B-cell lymphoma. Int J Hematol. 2018;107:194-200. doi:10.1007/s12185-017-2337-7.
97. Othman MF, Mitry NR, Lewington VJ, Blower PJ, Terry SY. Re-assessing gallium-67 as a therapeutic radionuclide. Nucl Med Biol. 2017;46:12-8. doi:10.1016/j.nucmedbio.2016.10.008.
98. Othman MFB, Verger E, Costa I, Tanapirakgul M, Cooper MS, Imberti C, et al. In vitro cytotoxicity of Auger electron-emitting [Nucl Med Biol. 2020;80-81:57-64. doi:10.1016/j.nucmedbio.2019.12.004.
99. Banfalvi G. Role of parathymic lymph nodes in metastatic tumor development. Cancer Metastasis Rev. 2012;31:89-97. doi:10.1007/s10555-011-9331-y.
100. Gerber SA, Rybalko VY, Bigelow CE, Lugade AA, Foster TH, Frelinger JG, et al. Preferential attachment of peritoneal tumor metastases to omental immune aggregates and possible role of a unique vascular microenvironment in metastatic survival and growth. Am J Pathol. 2006;169:1739-52. doi:10.2353/ajpath.2006.051222.
101. Lee W, Ko SY, Mohamed MS, Kenny HA, Lengyel E, Naora H. Neutrophils facilitate ovarian cancer premetastatic niche formation in the omentum. J Exp Med. 2019;216:176-94. doi:10.1084/jem.20181170.
102. Kitayama J, Emoto S, Yamaguchi H, Ishigami H, Watanabe T. CD90+ mesothelial-like cells in peritoneal fluid promote peritoneal metastasis by forming a tumor permissive microenvironment. PLoS One. 2014;9:e86516. doi:10.1371/journal.pone.0086516.
103. Levy AD, Shaw JC, Sobin LH. Secondary tumors and tumorlike lesions of the peritoneal cavity: imaging features with pathologic correlation. Radiographics. 2009;29:347-73. doi:10.1148/rg.292085189.
104. Smith TA. FDG uptake, tumour characteristics and response to therapy: a review. Nucl Med Commun. 1998;19:97-105. doi:10.1097/00006231-199802000-00002.
105. Huang H, Xiao F, Han X, Zhong L, Zhong H, Xu L, et al. Correlation of pretreatment 18F-FDG uptake with clinicopathological factors and prognosis in patients with newly diagnosed diffuse large B-cell lymphoma. Nucl Med Commun. 2016;37:689-98. doi:10.1097/MNM.0000000000000496.
106. Hirose Y, Suefuji H, Kaida H, Hayakawa M, Hattori S, Kurata S, et al. Relationship between 2-deoxy-2-[(18)F]-fluoro-d-glucose uptake and clinicopathological factors in patients with diffuse large B-cell lymphoma. Leuk Lymphoma. 2014;55:520-5. doi:10.3109/10428194.2013.807509.
107. Chang MC, Chen JH, Liang JA, Huang WS, Cheng KY, Kao CH. PET or PET/CT for detection of peritoneal carcinomatosis: a meta-analysis. Clin Nucl Med. 2013;38:623-9. doi:10.1097/RLU.0b013e318299609f.
108. Kim SJ, Lee SW. Diagnostic accuracy of. Br J Radiol. 2018;91:20170519. doi:10.1259/bjr.20170519.
109. Cunha L, Horvath I, Ferreira S, Lemos J, Costa P, Vieira D, et al. Preclinical imaging: an essential ally in modern biosciences. Mol Diagn Ther. 2014;18:153-73. doi:10.1007/s40291-013-0062-3.
110. Wong KP, Sha W, Zhang X, Huang SC. Effects of administration route, dietary condition, and blood glucose level on kinetics and uptake of 18F-FDG in mice. J Nucl Med. 2011;52:800-7. doi:10.2967/jnumed.110.085092.
111. Kim C, Kim IH, Kim SI, Kim YS, Kang SH, Moon SH, et al. Comparison of the Intraperitoneal, Retroorbital and per Oral Routes for F-18 FDG Administration as Effective Alternatives to Intravenous Administration in Mouse Tumor Models Using Small Animal PET/CT Studies. Nucl Med Mol Imaging. 2011;45:169-76. doi:10.1007/s13139-011-0087-7.
112. Schiffer WK, Mirrione MM, Dewey SL. Optimizing experimental protocols for quantitative behavioral imaging with 18F-FDG in rodents. J Nucl Med. 2007;48:277-87.
113. Aung W, Jin ZH, Furukawa T, Claron M, Boturyn D, Sogawa C, et al. Micro-positron emission tomography/contrast-enhanced computed tomography imaging of orthotopic pancreatic tumor-bearing mice using the $\alpha v\beta_3$ integrin tracer ^{64}Cu-labeled cyclam-RAFT-c(-RGDfK-)$_4$. Mol Imaging. 2013;12:376-87.

114. Yoshii Y, Matsumoto H, Yoshimoto M, Oe Y, Zhang MR, Nagatsu K, et al. Cu-Intraperitoneal Radioimmunotherapy: A Novel Approach for Adjuvant Treatment in a Clinically Relevant Preclinical Model of Pancreatic Cancer. J Nucl Med. 2019;60:1437-43. doi:10.2967/jnumed.118.225045.
115. Lee HJ, Tantawy MN, Nam KT, Choi I, Peterson TE, Price RR. Evaluation of an intraperitoneal ovarian cancer syngeneic mouse model using 18F-FDG MicroPET imaging. Int J Gynecol Cancer. 2011;21:22-7. doi:10.1097/IGC.0b013e3182021bda.
116. DeBerardinis RJ, Chandel NS. Fundamentals of cancer metabolism. Sci Adv. 2016;2:e1600200. doi:10.1126/sciadv.1600200.
117. Schmidt KC, Smith CB. Resolution, sensitivity and precision with autoradiography and small animal positron emission tomography: implications for functional brain imaging in animal research. Nucl Med Biol. 2005;32:719-25. doi:10.1016/j.nucmedbio.2005.04.020.
118. Fanchon LM, Dogan S, Moreira AL, Carlin SA, Schmidtlein CR, Yorke E, et al. Feasibility of in situ, high-resolution correlation of tracer uptake with histopathology by quantitative autoradiography of biopsy specimens obtained under 18F-FDG PET/CT guidance. J Nucl Med. 2015;56:538-44. doi:10.2967/jnumed.114.148668.
119. Dedrick RL, Myers CE, Bungay PM, DeVita VT. Pharmacokinetic rationale for peritoneal drug administration in the treatment of ovarian cancer. Cancer Treat Rep. 1978;62:1-11.
120. Sugarbaker PH. Cytoreductive surgery and hyperthermic intraperitoneal chemotherapy in the management of gastrointestinal cancers with peritoneal metastases: Progress toward a new standard of care. Cancer Treat Rev. 2016;48:42-9. doi:10.1016/j.ctrv.2016.06.007.
121. Flood M, Narasimhan V, Waters P, Ramsay R, Michael M, Warrier S, et al. Survival after cytoreductive surgery and hyperthermic intraperitoneal chemotherapy for colorectal peritoneal metastases: A systematic review and discussion of latest controversies. Surgeon. 2020. doi:10.1016/j.surge.2020.08.016.
122. Liu H, Carpenter CM, Jiang H, Pratx G, Sun C, Buchin MP, et al. Intraoperative imaging of tumors using Cerenkov luminescence endoscopy: a feasibility experimental study. J Nucl Med. 2012;53:1579-84. doi:10.2967/jnumed.111.098541.

7. sz. melléklet

DOKTORI ÉRTEKEZÉS BENYÚJTÁSA ÉS NYILATKOZAT A DOLGOZAT EREDETISÉGÉRŐL

Alulírott

név: Dr. Ritter Zsombor

születési név: Ritter Zsombor

anyja neve: Kiss Gabriella Erika

születési hely, idő: Pécs, 1991.03.06.

Clinical and experimental molecular and multimodality imaging studies in B cell malignant lymphomas című doktori értekezésemet a mai napon benyújtom a(z)

PTE ETK Doktori Iskola

Onkológia-Egészségtudopmány 0-2-8 Programjához/témacsoportjához

Témavezető(k) neve: Prof. Dr. Zámbó Katalin, Dr. Alizadeh Hussain

Egyúttal nyilatkozom, hogy jelen eljárás során benyújtott doktori értekezésemet
- korábban más doktori iskolába (sem hazai, sem külföldi egyetemen) nem nyújtottam be,
- fokozatszerzési eljárásra jelentkezésemet két éven belül nem utasították el,
- az elmúlt két esztendőben nem volt sikertelen doktori eljárásom,
- öt éven belül doktori fokozatom visszavonására nem került sor,
- értekezésem önálló munka, más szellemi alkotását sajátomként nem mutattam be, az irodalmi hivatkozások egyértelműek és teljesek, az értekezés elkészítésénél hamis vagy hamisított adatokat nem használtam.

Dátum: 2022.08.31.

.....
doktorjelölt aláírása

Zámbó Katalin
.....
témavezető aláírása

.....
társtémavezető aláírása